國立臺灣大學電機資訊學院光電工程學研究所

碩士論文

Graduate Institute of Photonics and Optoelectronics

College of Electrical Engineering and Computer Science

National Taiwan University

Master Thesis

癌細胞對金奈米環攝取行為與侷域表面電漿子共振導

致細胞滅活的效率

Cancer Cell Uptake Behavior of Au Nanoring and Its

Localized Surface Plasmon Resonance Induced Cell

Inactivation Efficiency

褚哲寬

Che-Kuan Chu

指導教授：楊志忠 博士

Advisor: C. C. Yang, Ph.D.

中華民國 103 年 7 月

July 2014

誌謝

本論文的完成，首先要感謝我的指導教授楊志忠博士，於我的碩士班期間不斷淬煉我的研究能力，使我獲得專業知識，習得研究方法，並在實驗設備上給予充分的支持。感謝口試委員-江衍偉教授、孫家偉教授、陳顯禎教授，在論文內容給予指導，使本論文可以更臻完備。

在碩士班研究期間，我要特別感謝實驗室的所有成員與光電所夥伴們在研究與生活上的幫助: 之耕、師揚、祐維、毅洲、廷達、文彥及其他成員，在此感謝你們。另外感謝:文峰、佳憲及其他所外前輩與夥伴們在我研究上的協助。感謝實驗室助理張珮、尚音伶、柯信鈺等，給予行政業務的幫助。

最後，我要感謝我的父母與家人，褚志清先生，石維麗女士，在生活上與精神上的支持，使我能專心於研究，順利完成碩士學位。謹將此論文獻給我的父母與家人，表達我最誠摯的感激。

中文摘要

在本論文中，我們將侷域表面電漿子共振波長為 1058 奈米的金奈米環分成生物鍵結上針對 SAS 口腔癌細胞膜上受體的抗體和未鍵結兩組，加到培養皿中與此癌細胞培養，隨後以波長為 1065 奈米的雷射激發金奈米環的侷域表面電漿子共振，利用其產生的光熱效應使癌細胞死亡。透過不同金奈米環加入癌細胞的培養時間，我們可得到不同細胞攝取金奈米環的數量，進而得到不同滅活細胞所需最小的臨界雷射強度。對於每個培養時間，我們試著利用感應耦合電漿質譜分析儀去測量吸附在細胞膜上和被內化入細胞的金奈米環的數量和攝取的百分比，為達到此目的，我們收集以生理食鹽水沖洗細胞的殘餘液得到懸浮的金含量，以碘化鉀和碘的混合液將吸附在細胞膜表面的奈米環蝕刻，以生理食鹽水沖洗收集得到吸附在細胞膜的金含量，並以細胞溶液來得到內吞的金含量，透過掃描式電子顯微鏡估量出奈米環之大小，進而分析出此三部分的金奈米環數量。我們以圈圖的方式估算出在不同雷射強度照射下，在沖洗前，沖洗後，以及金蝕刻後的臨界雷射強度。對於其上有抗體的金奈米環，癌細胞攝取的速度較快，且隨著時間的增加，細胞內吞的金奈米環的量越多。但觀察吸附在細胞膜上的金奈米環，發現加入金奈米環後十二小時達到峰值。對

於其上沒有抗體鍵結的金奈米環，細胞攝取的速度較慢，在同樣時間下攝取金奈米環的量明顯較少，且吸附在細胞膜上的奈米環的數量在二十小時後才達到峰值。以吸附和內吞的金奈米環和臨界雷射強度交叉比對後，我們發現吸附的金奈米環對於細胞滅活的效果較好。當細胞吸附最多金奈米環時會得到最小臨界雷射強度。
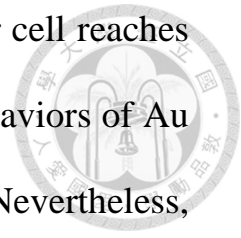
Abstract
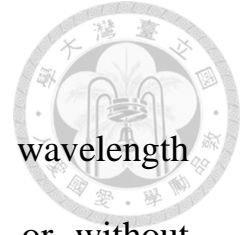
Au nanorings (NRIs), which have the LSP resonance wavelength around 1058 nm, either with linked antibody (NRI-AB) or without antibody (NRI-control), are applied to SAS oral cancer cell for cell inactivation through the localized surface plasmon (LSP)-induced photothermal effect when it is illuminated by a laser of 1065 nm in wavelength. Various incubation times after the application of Au NRIs to cell are considered for observing the variations of cell uptake of Au NRI and hence the threshold laser intensity for cancer cell inactivation. In each case of incubation time, the SAS cell is washed for evaluating the Au NRI number per cell adsorbed and internalized by the cells. Also, the Au NRIs adsorbed (remaining on cell membrane) are etching with KI/I_2 to evaluate the Au NRI number per cell internalized by the cells. The threshold laser intensities before washout, after washout, and after KI/I_2 etching are calibrated from the circular area sizes of inactivated cells around the illuminated laser spot center under the illuminations of various laser power levels. The adsorbed and internalized Au NRIs per cell are obtained from inductively coupled plasma mass spectrometry measurements of the flushed solution in the KI/I_2 etching process and the remaining cell solution, respectively. By using Au NRIs with antibody, it is found that the internalized Au NRI number per cell increases with

incubation time. However, the adsorbed Au NRI number per cell reaches a maximum at 12 hrs in incubation time. The cell uptake behaviors of Au NRIs without antibody are similar to those with antibody. Nevertheless, the NRI numbers per cell are significantly smaller. Meanwhile, the incubation time for the maximum adsorbed NRI number per cell is delayed to 20 hrs. By comparing the variation of threshold laser intensity for cell inactivation, it is found that the adsorbed NRIs can cause more effective cancer cell inactivation, when compared with the internalized NRIs. The minimum threshold laser intensities after cell solution washout in either case with or without antibody are observed before KI/I_2 etching under the aforementioned incubation time conditions of maximum adsorbed NRI number per cell.

Content

Chapter 1

Introduction

1.1 Localized Surface Plasmon

Localized surface plasmon (LSP) represents the local oscillation of free electrons on a metal nanoparticle (NP). Unlike the excitation mechanism of surface plasmon polariton (SPP), LSP has a broad distribution of wavevector [1], such that it can be excited and can radiate in a broad range of direction. Figure 1.1 shows the dispersion relations of SPP and LSP. One can see that due to the momentum mismatch between SPP dispersion and light line, light extraction from SPP energy needs certain mechanisms to match the momentum, such as prism, grating or rough surface structures. In contrast, the dispersion relation curve of LSP crosses the light line, such that there is no need to match the momentum for the energy exchange between light and LSP. Such optical properties make LSP a good choice for the applications to light energy exchange. For example, light scattering for bio-image contrast enhancement and light absorption for photothermal applications are widely used. LSPs can exist on rough metallic surfaces, aggregates and clusters of metal

nanoparticles, as well as engineered metal nanostructures. The resonance frequency of an LSP can be tuned by controlling the size and shape of a metal nanoparticle (NP) and the refractive index of its surrounding medium. They can create strong localized electromagnetic field. At its resonance, LSP can induce enhanced scattering and absorption of a metal NP.

When an electromagnetic wave propagates through a metal NP, the energy of such an electromagnetic wave can be scattered or absorbed by the NP through LSP resonance and result in its extinction. For a homogeneous metal nanosphere, which is surrounded by an isotropic dielectric medium, as shown in Fig. 1.2, by using the quasi-static approximation, the corresponding scattering and absorption cross sections of an incident light can be written as [2]:

$$C_{Sca} \cong \frac{8\pi}{3} k^4 a^6 \left| \frac{\epsilon_1(\omega) - \epsilon_2(\omega)}{\epsilon_1(\omega) + 2\epsilon_2(\omega)} \right|^2 \qquad (1.1)$$

$$C_{Abs} \cong 4\pi k a^3 \operatorname{Im}\left[\frac{\epsilon_1(\omega) - \epsilon_2(\omega)}{\epsilon_1(\omega) + 2\epsilon_2(\omega)} \right] \qquad (1.2)$$

$$\text{with } k = \frac{2\pi}{\lambda}$$

Here, $\epsilon_1(\omega)$ and $\epsilon_2(\omega)$ are the complex dielectric constants of the metal nanosphere and the surrounding medium, respectively. Equations (1.1) and (1.2) show the strong dependence of the resonance frequency on the surrounding dielectric constant. Such a strong dependence on the

surrounding dielectric constant makes metal NPs the ideal choice for the refractive index sensing applications. In using the LSP resonance features in biomedical applications, Au NPs are preferred due to their biocompatibility and flexibility to conjugate biomolecules. The widely used Au NPs for biomedical applications include sphere-like solid Au NPs [3], nanorods [4-6], silica/Au nanoshells [7-9], hollow Au NPs [10, 11], and nanocages [12-14]. However, the wavelengths of the major LSP resonance modes of those Au NPs of high quality are usually shorter than 900 nm. In biomedical applications, due to weaker tissue absorption and scattering, the use of a light source with the wavelength longer than 950 nm can result in deeper tissue penetration for extending the depth ranges of diagnosis and therapy [15]. Figure 1.3 shows the relative absorption and scattering spectra of tissue, indicating clearly the deeper light penetration into tissue in the window of 950-1300 nm. Therefore, Au nanorings (NRIs) with the LSP resonance wavelengths longer than 1000 nm show their advantages of deeper-tissue biomedical application.

1.2 Review of Gold Nanoparticle

1.2.1 Gold Nanosphere

Among those Au NPs used in biomedical applications, Au nanosphere has the simplest shape and is the first Au NP developed by

human. By now, Au nanosphere is still the most widely used Au NP in biomedical applications due to its relative simple synthesis process. The most popular method of producing Au nanospheres is based on the " Turkevitch method ", which was first developed in 1951 by Turkevitch [16-18]. In this method, Au nanospheres are formed from the reduction of $HAuCl_4$ in water with citrate as a reducing agent. The presence of citrate also serves as an anionic stabilizer to prevent the particles from aggregation in solution. The reaction equation for this method can be written as follows:

$$6AuCl_4^- + C_6H_8O_7 + 5H_2O \rightarrow 6Au^0 + 6CO_2 + 24Cl^- + 18H^+ \quad (1.3)$$
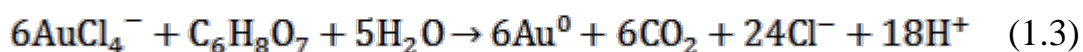
By using this method, the size of gold nanospheres can be tuned from 15 to 150 nm by controlling the ratio of citrate to $HAuCl_4$. For further reducing the size of Au nanospheres, Brust et al. demonstrated a method to produce 1-3 nm Au NPs by using borohydride reduction of Au salt with alkanethiol capping agent [18, 20]. In 2001, N. R. Jana et al. developed a seeding growth approach to prepare high quality (standard deviation ~ 10-15%) Au nanospheres with the size between 5 and 40 nm [21] . Figure 1.4(a) shows a typical TEM image of the Au nanospheres with the average size at 99 nm [22]. One can see that the shape of Au nanospheres is slightly different from a true spherical shape.

The LSP properties of Au nanospheres can be described by the Mie

theory with the quasi-static approximation, as mentioned in section 1.1. In this approximation, the extinction cross section of an incident light can be written as [23]:

$$C_{Ext} \cong \frac{18\pi V \epsilon_d^{3/2}}{\lambda} \frac{\epsilon_2(\omega)}{\left(\epsilon_1(\omega) + 2\epsilon_d(\omega)\right)^2 + \epsilon_2(\omega)^2} \; . \tag{1.4}$$

Here, $\epsilon(\omega) = \epsilon_1(\omega) + i\epsilon_2(\omega)$ is the complex dielectric constant of the metal particle, V is the volume of the nanosphere. ϵ_d is the dielectric constant of the surrounding medium. The maximum value can be obtained under the condition of $\epsilon_1(\omega) = -2\epsilon_d(\omega)$. This is the LSP resonance peak of a metal nanosphere in a dielectric medium. For tuning the LSP resonance wavelength of an Au nanosphere, the only parameter available in experiment is its size. Figure 1.4(b) shows the extinction spectra of Au nanospheres of 9, 22, 48, and 99 nm in diameter within water [22]. One can see that with increasing particle size (9 to 99 nm), the LSP resonance peak is red shifted from 517 to 575 nm. Normally, the LSP resonance wavelength of a sphere-like NP is limited to the visible range. Such NPs are not suitable for deep tissue applications because of the shallow penetration of visible light.

1.2.2 Gold Nanorod

Au nanorod (NR) is the first practical gold NP which pushes the LSP resonance into the infrared range in biomedical applications. Unlike a

spherical Au NP, the asymmetric shape of Au NR can split the LSP resonance mode due to different excitation orientations of the rod with respect to the electric field of incident light. When the shape of an Au NP changes from sphere to rod, the LSP resonance band is split into two bands. According to Gan's theory, which was predicted by Gan to describe the SP resonance properties of a rod-shaped particle in 1912, the extinction coefficient α can be expressed as [24]:

$$\alpha = \frac{2\pi N V \varepsilon_m^{3/2}}{3\lambda} \sum_j \frac{\left(\frac{1}{P_j^2}\right)\varepsilon_2}{\left(\varepsilon_1 + \frac{1-P_j}{P_j}\varepsilon_m\right)^2 + \varepsilon_2^2}. \tag{1.5}$$

Here, V is the volume of the nanorod, N is the number of particles per unit volume, λ is the wavelength of the incident light, $\varepsilon = \varepsilon_1 + i\varepsilon_2$ is the complex dielectric constant of the metal, and ϵ_m is the dielectric constant of the surrounding medium. Pj (j = A, B, C; in rod-shape, A is the length, B = C is the width) are the depolarization factors of the rod, which is defined as:

$$P_A = \frac{1-e^2}{e^2}\left[\frac{1}{2e}\ln\left(\frac{1+e}{1-e}\right) - 1\right], \tag{1.6}$$

$$P_B = P_C = \frac{1-P_A}{2}, \tag{1.7}$$

where e is the rod ellipticity, which is described by:

$$e^2 + \left(\frac{1}{\eta}\right)^2 = 1 \tag{1.8}$$

In this equation, $\eta = A/B$ is the aspect ratio of the NR. The LSP resonance peak of an NR with any aspect ratio can be calculated by using these equations.
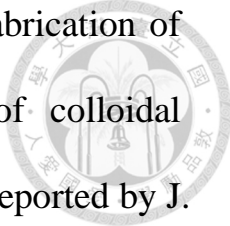
A number of methods have been developed for preparing Au NRs, including the photochemical reduction method [25], template-directed method [26], electrochemical method [27], and seed-mediated growth method [28]. The seed-mediated growth method reported by Murphy and co-workers in 2005 is a popular protocol for preparing Au NRs. The process starts with a reduction procedure of $HAuCl_4$ with sodium borohydride ($NaBH_4$) in the presence of citrate. This step forms a solution of 3.5 nm Au NPs, which serve as the seed particles of the following reduction processes. Then, the seed solution is mixed with a growth solution containing $HAuCl_4$, $C_{16}TAB$, and ascorbic acid to generate Au NRs. Figure 1.5(a) shows a typical TEM image of Au NRs prepared with the seed-mediated growth method. One can see that Au nanospheres are also generated besides the Au NRs during the synthesis processes. The uniformity of Au NRs can be improved by removing those nanospheres through centrifugation. The LSP resonance wavelength of Au NRs can be tuned by changing their aspect ratios, which can be controlled by the synthesis recipes such as synthesis time. Even though lots of Au NRs with different aspect ratios may be synthesized during a synthesis process, the separation technique based on centrifugation can be used to collect Au

NRs of similar aspect ratios. Figure 1.5(b) shows the TEM image of Au NRs with the aspect ratio around 3, the LSP resonance peak around 700 nm [29]. Figure 1.5(c) shows the extinction spectra of Au NRs with the aspect ratios at 1.7, 2.8, 3.5, 4.0, and 4.4 [29]. In this figure, the major extinction peaks on the long-wavelength side are caused by the longitudinal LSP mode. The lower extinction peaks on the short-wavelength side are due to the transverse LSP mode. One can see that with increasing aspect ratio, the LSP resonance wavelength of the longitudinal LSP mode is red-shifted largely from the visible range (aspect ratio = 1.7, peak at ~600 nm) into the near-infrared range (aspect ratio = 4.4, peak at ~850 nm). Although an Au NR of a larger aspect ratio can push the LSP resonance wavelength into the spectral range around 1300 nm, it is usually difficult to control the uniformity of nanorods and hence the application becomes unreliable.

1.3 Characteristics of Gold Nanoring

Au nanoring (NRI) is an axial symmetric nanostructure that is usually fabricated on a substrate with the semiconductor nano-process techniques. Comparing with other colloidal Au NPs, such as NR and NS, an Au NRI has more control parameters to adjust their LSP resonance peak, including ring diameter, ring thickness, and ring height. Hence, Au NRIs have higher flexibility in designing its geometry and can have better

control in geometry parameter, uniformity, and yield. The fabrication of Au NRIs on a substrate was based on the methods of colloidal lithography and secondary sputtering of Au, which was first reported by J. Aizpurua et al. in 2003 [30]. Other researches and the applications of on-substrate Au NRIs in molecular sensing have also been demonstrated by the same group in the past few years [31, 32]. In 2010, our group demonstrated the fabrication of Au NRIs on a sapphire substrate and then the transfer of the NRIs into water solution for illustrating the photothermal effect and imaging contrast enhancement [33, 34]. Recently, we further demonstrated the on-substrate fabrication of a bio-conjugated Au NRI solution based on nano-imprint lithography. In this study, we will illustrate the effects of photothermal therapy through LSP resonance-induced absorption enhancement by applying the bio-conjugated Au NRIs to human oral cancer cells and illuminating the cells with a laser of 1060 nm in wavelength [35]. Furthermore, by applying KI/I_2 solution, which is usually used in semiconductor process to etch surface Au, we can determine the efficiencies of the internalized and adsorbed Au NRIs to cell inactivation. Although Au NRIs can also be fabricated in solution by chemical synthesis [37, 38], it is difficult to produce high quality and well controlled shape of Au NRIs. Besides, the on-substrate fabricated Au NRIs has the advantages in biomedical applications because their bio-conjugation procedures can be undertaken

when Au NRIs are still attached on a substrate. In this situation, we can simply immerse the sample substrate in the reaction solution and then rinse it in DI water to remove the residues. The advantages of NRI bio-conjugation on a substrate include simple and fast process, effective removal of residues, and avoidance of NP loss in the centrifuge process and minimization of NP aggregation in the bio-conjugation process.

The fundamental LSP resonance mode of a ring structure is the cross-ring dipole mode, which has been reported by J. Aizpurua et al. in 2003 [30]. Figures 1.6(a) and 1.6(b) show the near field distribution and field enhancement of the LSP dipole mode in a ring structure [30]. One can see that the electric field is greatly enhanced inside the ring cavity, where the field is quite homogeneous. Similar to an Au NS, the resonance wavelength of the LSP dipole mode of an Au NRI is dependent on its size and the aspect ratio of the ring radius to thickness. With increasing aspect ratio of an Au NRI, the LSP resonance peak is red-shifted significantly in the infrared range. In addition, the LSP resonance wavelength of the cross-ring dipole mode can also be controlled by the ring height. Figure 1.7 shows the simulation results of the LSP resonance wavelengths of the cross-ring dipole modes and the axial dipole modes (resonant along the ring axis) as functions of ring height, H, and ring thickness, d. The outer radius of the NRI is fixed at a = 50 nm [36]. For a fixed ring thickness, the resonance wavelength of the cross-ring dipole mode decreases with

increasing in ring height. On the other hand, that of the axial dipole mode increases with increasing ring height.
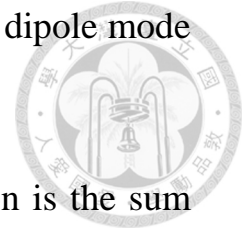
As discussed in Section 1.1, the extinction cross-section is the sum of scattering and absorption cross-sections. For a ring structure, the scattering and absorption cross-sections can be changed by tuning the geometry parameters such as ring size, ring height, and the aspect ratio. Figure 1.11 shows the simulation results of Au NRIs with the outer radii at a = 37.5, 62.5, and 87.5 nm in the top, middle, and bottom panels, respectively. The red dashed curve and blue solid curve in the panels represent absorption and scattering cross-sections, respectively. The five sets of curve in each panel with their peaks shifting from short to long wavelength correspond to 2.5, 3.33, 5, 6.67, and 10 in aspect ratio. We can see that for the NRIs with the same aspect ratio, the absorption is dominant in the extinction cross-section when the NRI has a smaller size. In contrast, the scattering cross-section increases significantly when the the NRI size becomes larger. On the other hand, for the NRIs with the same outer radii, the increase of the aspect ratio of NRI will cause the decrease of absorption cross-section and enlarge the scattering cross-section simultaneously. The values of scattering and absorption cross sections can be controlled by the geometry parameters of NRI, which can be designed for a specific application. For example, an NRI with a larger scattering cross-section is suitable for the application of
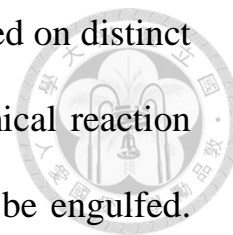
scattering-based image contrast enhancement. On the other hand, the photothermal-based applications need an NRI with a larger absorption cross-section. Such high flexibility in controlling its optical properties makes Au NRI a good platform for both scattering- and absorption-based applications.
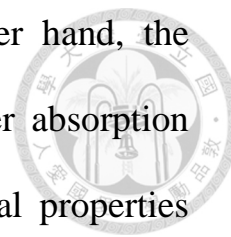
1.4 Process of Cell Uptake of Au NPs

There are three main pathways for materials to naturally enter cells: active transport, phagocytosis, and pinocytosis. Active transport is the movement of molecules across a cell membrane in the direction against their concentration gradient, like moving from a low concentration to a high concentration (see Fig. 1.12(a)). Active transport is usually associated with accumulating high concentrations of molecules that the cell needs, such as ions, glucose and amino acids. Active transport uses cellular energy, such as ATP, unlike passive transport, which does not use cellular energy. Examples of active transport include the uptake of glucose in the intestines in humans and the uptake of mineral ions into root hair cells of plants. Phagocytosis is the process by which a cell (often a phagocyte or a protist) engulfs a solid particle to form an internal vesicle known as a phagosome (see Fig. 1.12(b)). The process of phagocytosis begins as soon as the cell identifies a nearby cell or particle

as one that it needs to engulf. This identification is often based on distinct proteins on the surface of the pathogenic cell or by a chemical reaction between a receptor on the cell's surface and the particle to be engulfed. The cell begins the phagocytosis process by forming a furrow in the cell membrane. The membrane flows around the particle or cell until it completely surrounds it, and then it pinches off, leaving the particle inside the cell, surrounded by a pouch called a phagosome, which is formed from a portion of the cell membrane. Next, cell organelle known as lysosome fuses with the phagosome, releasing enzyme to break down the cell or particle that it contains. Pinocytosis is a mode of endocytosis in which small particles are brought into the cell, forming an invagination, and then suspended within small vesicles (see Fig. 1.12(c)). In contrast to phagocytosis, it generates very small amounts of ATP from the wastes of alternative substances such as lipids. Pinocytosis is nonspecific in the substances that it transports. The cell takes in surrounding fluids, including all solutes present.

Unlike these pathways, there are some researches that refer that if the surface of Au NP is coated with some proteins that can target to specific receptor on cell membranes, Au NPs can enter cells mainly through receptor-mediated endocytosis (RME), which is the case of our bio-conjugated Au NRIs [36]. Receptor-mediated endocytosis, also called clathrin-dependent endocytosis, is a process by which cells internalize

molecules by the inward budding of plasma membrane vesicles containing proteins with receptor sites specific to the molecules being internalized (see Fig. 1.12(d)).
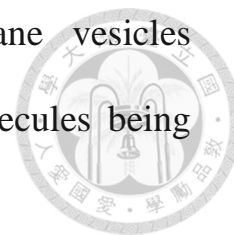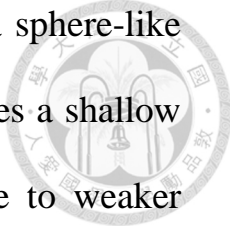
The process of receptor-mediated endocytosis is strongly affected by the geometry of Au NPs. There are many factors, such as the membrane stretching, the ratio of adhesion, the bending energy of cell membrane, may be involved in the question of why size affects the uptake of Au NPs. All these factors are strongly associated with the so-called "wrapping time", which describes how long a membrane encloses a particle [39, 40]. Gao et al. has also referred that the wrapping time depends on particle size. The cellular uptake can be considered only as a result of competition between thermodynamic driving force for wrapping and the receptor diffusion kinetics. These two factors will determine how fast and how many NPs are taken up by a cell. The first term refers to the amount of free energy needed to drive the NPs into the cell. The second term refers to the kinetics of recruitment of receptors to the binding site. NP that is small, like smaller than 50 nm, will not produce sufficient free energy for causing a invagination that is enough to wrap the NPs on the surface of the membrane. In this case, endocytosis cannot happen. However, as
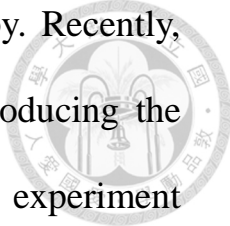
shown in Fig. 1.13, for smaller NPs to enter the cell, they can require higher free energy by aggregation and the cell membrane may wrap them all at once. For bigger NPs, like our Au NRIs (~100 nm), the wrapping time is slower because of the slower receptor diffusion kinetics, but larger particles can produce free energy needed for causing an invagination, see Fig. 1.14. This indicates that the number of internalized NPs becomes lower [39-41]. On the other hand, the number of adsorbed NPs becomes higher because the time that NPs binding onto the membrane is prolonged.

1.5 Photothermal Therapy

The LSP-resonance enhanced absorption of Au NPs attached to or taken up by targeted cancer cells can result in local heating and cause the apoptosis or necrosis of the cells, leading to the effect of hyperthermia therapy of cancer [42-51]. Compared to photoabsorbing dyes, the absorption cross section of the LSP resonance of Au NPs can be four to five orders of magnitude larger. Therefore, Au NP with LSP resonance becomes an effective photothermal therapy agent. For photothermal application, the commonly used Au NPs include sphere-like solid Au NPs [3], nanorods [4-6], silica/Au nanoshells [7-9], hollow Au NPs [10, 11],

and nanocages [12-14]. The LSP resonance wavelength of a sphere-like solid Au NP is limited in the visible range [52], which implies a shallow application depth of tissue. In biomedical applications, due to weaker tissue absorption and scattering, the use of a light source with the wavelength between 950 and 1300 nm can result in deeper tissue penetration for extending the depth ranges of diagnosis and therapy [53]. Although an Au nanorod of a larger aspect ratio can push the LSP resonance wavelength into the spectral range around 1100 nm, it is usually difficult to control the uniformity and thermal stability of nanorods and hence the application becomes unreliable. Also, although theoretically nanoshells of thin Au layers can lead to LSP resonances at longer wavelengths, the non-uniform shell/wall thickness results in significantly broadened and hence weaker resonance peaks. Reliable Au NPs of other geometries for longer-wavelength and stronger LSP resonance are needed for further developments of targeted photothermal therapy. In this regard, an Au NRI can be used for extending the LSP resonance wavelength to the spectral range of 950-1300 nm for deeper tissue penetration. Bio-conjugated Au nanorods and nanoshells have been widely applied to cell and animal experiments to show the photothermal therapy effects [54]. Our group has also demonstrated the cancer cell inactivation effect by using our Au NRI samples [35]. Because of its high permeability in human body, bio-conjugated Au NPs can be easily
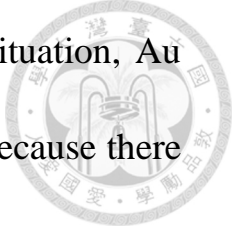
accumulated in a tumor, leading to effective targeted therapy. Recently, fluorescence molecules were also linked to Au NPs for producing the functions of diagnosis and therapy simultaneously. A mouse experiment with the combination of photothermal therapy and PDT has been undertaken to show effective suppression of tumor growth [55]. Besides, cancer drug delivery by Au NPs can lead to the combined effect of chemotherapy and photothermal therapy. A mouse experiment with Au-nanorod/chitosan hybrid NPs has demonstrated an improved therapeutics process [50]. The heating process can enhance the chemotherapy effect. Besides, because the photothermal effect of LSP resonance can produce local heating and hence local refractive index variation and/or local thermal expansion, it can also be monitored by OCT scanning [56]. Therefore, with OCT measurement, the photothermal effect can also be used for cancer cell labeling.

1.6 Research Motivations

With the advantages of scattering and absorption enhancement in the long-wavelength range that allows deeper tissue penetration [35], Au NRI is an effective agent for biomedical applications, like photothermal therapy and optical coherence tomography. However, limited by the fabrication process, the size of Au NRI is always between 90~180nm,

which is much larger than those of other Au NPs. In this situation, Au NRIs undergo a slow process of cell internalization [39-41] because there is there's a longer wrapping time for larger Au NPs. On the other hand, a larger NP has more antibodies bio-conjugated on the surface such that the adsorption probability of Au NRIs onto a cell is increased. With the considerations above, we believe that the study of the photothermal cell inactivation efficiency with internalized and adsorbed Au NRIs is needed. To distinguish the efficiencies of internalized and adsorbed Au NRIs in photothermal cell inactivation, KI/I_2 solution can be applied to etch Au NRIs adsorbed on the cell membrane. Through this process, we can compare the cell inactivation efficiency of internalized Au NRIs with that of adsorbed Au NRIs.
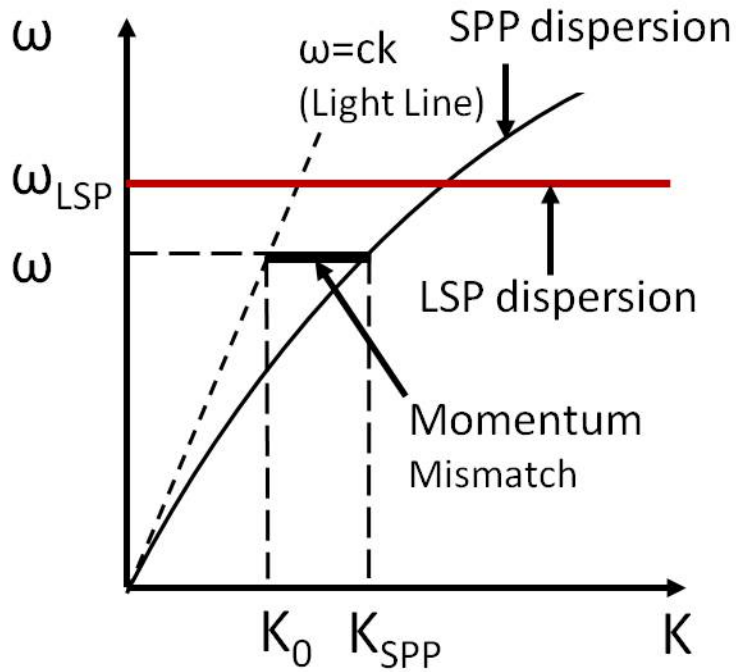
Fig. 1.1 Dispersion relations of SPP and LSP. Due to the momentum mismatch between SPP dispersion and light line, light extraction from SPP energy needs certain mechanisms to match the momentum, such as prism, grating or rough surface structures. In contrast, there is no need to match the momentum for the energy exchange between light and LSP.
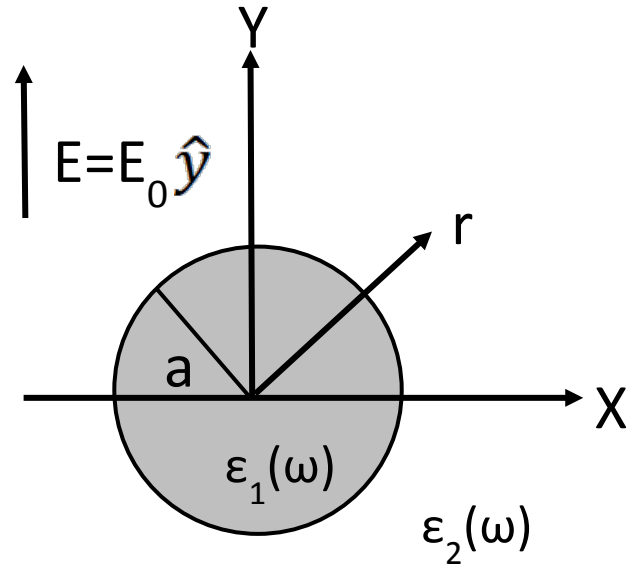
Fig. 1.2 Sketch of a homogeneous metallic sphere surrounded by an
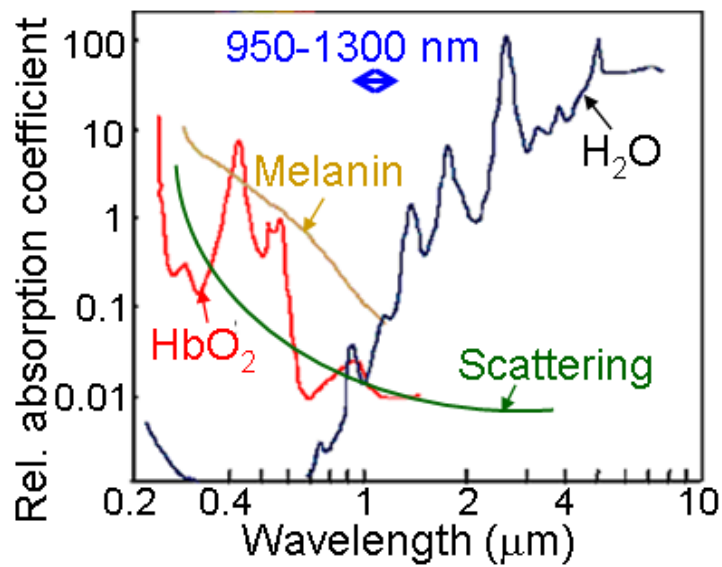
isotropic dielectric medium in a uniform static electric field.

Fig. 1.3 Relative absorption and scattering spectra of tissue.
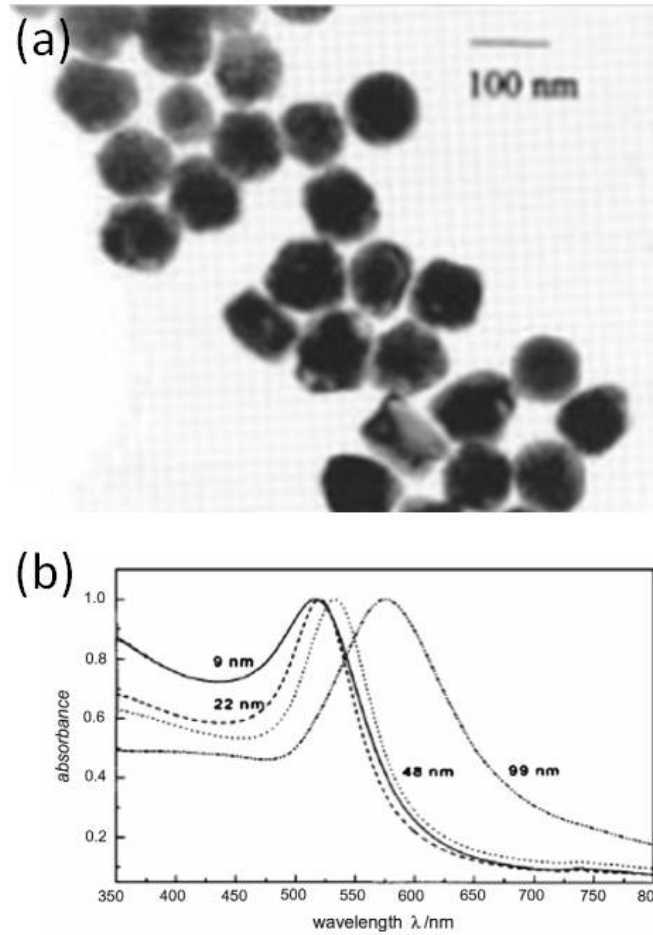
Fig. 1.4 (a) TEM image of Au nanospheres with the average size at 99

nm.(b) Extinction spectra of Au nanospheres of 9, 22, 48, and 99 nm

in diameter within water [22].
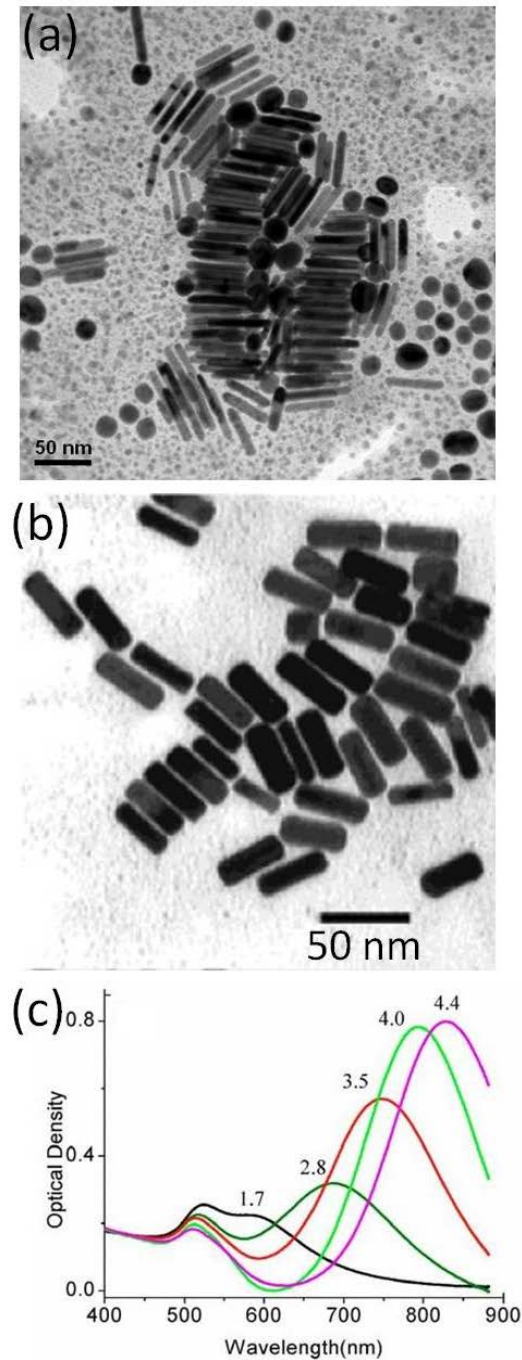
Fig. 1.5 (a) Typical TEM image of Au NRs prepared via the
seed-mediated growth method. (b) TEM image of Au NRs with the
aspect ratio around 3, the LSP resonance peak around 700 nm. (c)
Extinction spectra of gold nanorods with the aspect ratios at 1.7, 2.8,
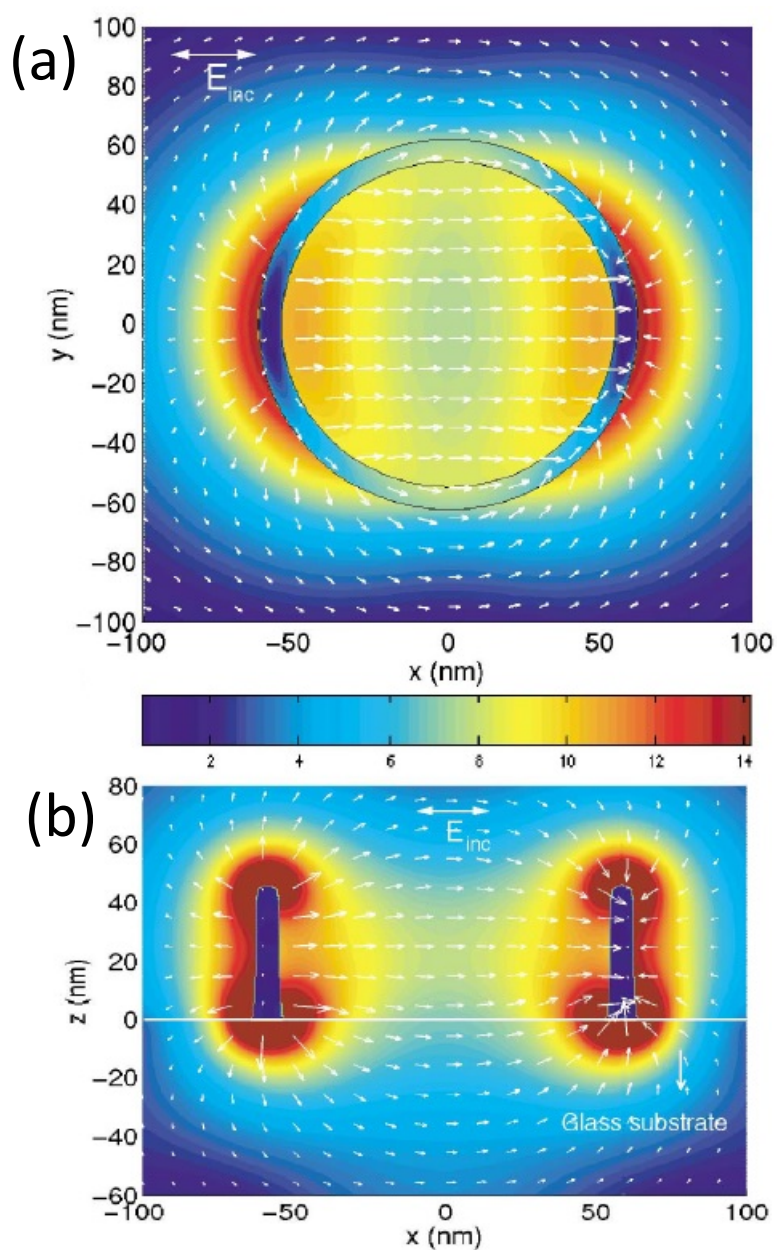3.5, 4.0, and 4.4, respectively [29].

Fig. 1.6 (a) Horizontal cut and (b) vertical cross section of the near field distribution and field enhancement of the LSP dipole mode in a ring structure (ring radius: 60 nm, ring thickness: 10 nm, ring height: 22.7 nm), the scale bar shows the field enhancement [36].
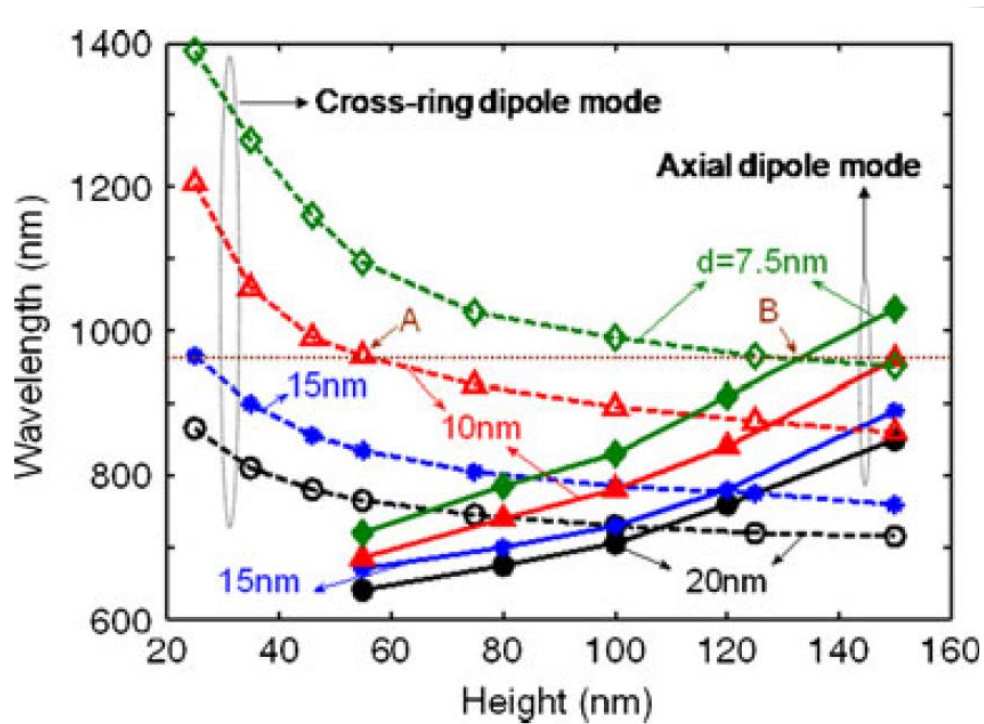
Fig. 1.7 Variations of LSP resonance wavelengths of the cross-ring dipole and axial dipole modes of an Au NRI as functions of the ring height, H, at various ring thicknesses, d, with the outer radius of the NRI fixed at a = 50 nm. The horizontal dotted line at 965 nm passes the intersection point of the two curves of d = 7.5 nm for the cross-ring and axial dipole modes [36].
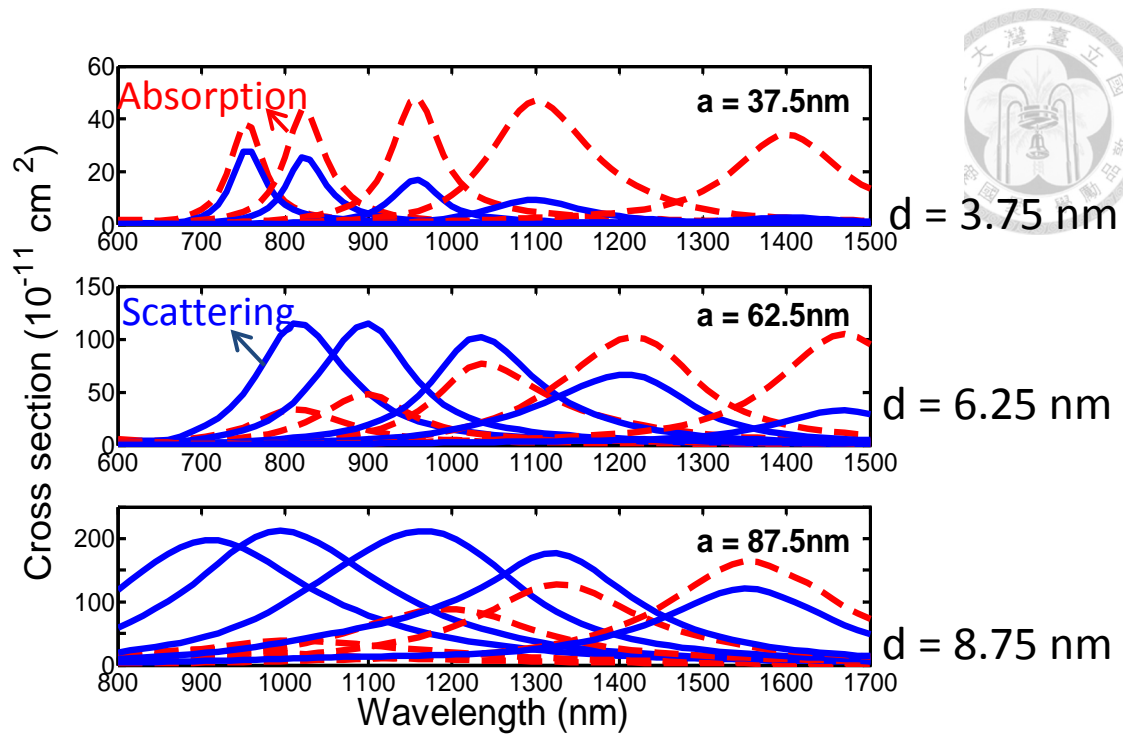
Fig. 1.11 Simulation results of Au nanorings with the outer radii at a =
37.5, 62.5, and 87.5 nm in the top, middle, and bottom panels,
respectively. The red dashed curve and blue solid curve in the panels
represent absorption and scattering cross-section, respectively. The five
sets of curve in each panel with their peaks shifting from short to long
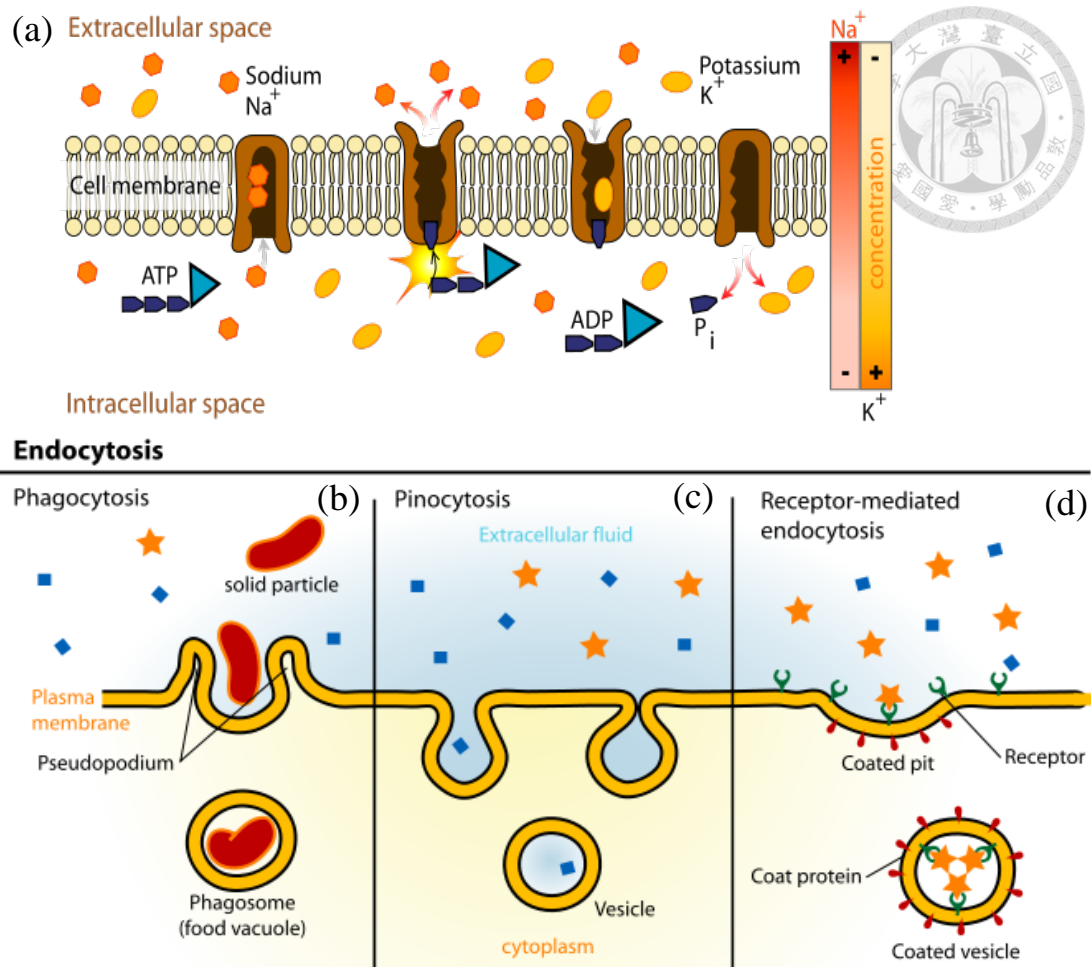wavelength correspond to 2.5, 3.33, 5, 6.67, 10 in aspect ratio.

Fig. 1.12 Four types of outer material entering into cell: (a) active transport, (b) phagocytosis, (c) pinocytosis, (d) receptor-mediated endocytosis. (pictures are downloaded from http://commons.wikimedia.org/wiki/File:Endocytosis_types.svg)
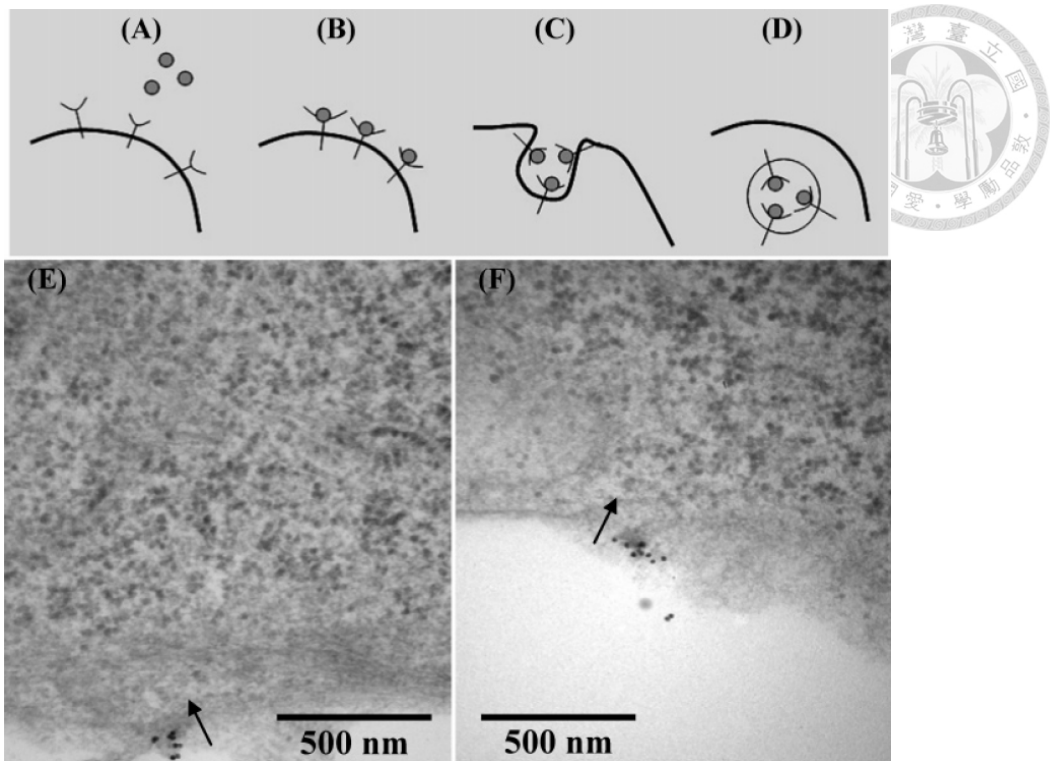
Fig. 1.13 Different stages of the cellular uptake process of _14 nm transferrin-coated Au NPs. (A-D) Schematic depicting the arrival of a NP at the cell membrane, binding of the nanopartcles to surface receptors, membrane wrapping of the NP, and finally internalization into the cell, respectively. (E-F) TEM images capturing each of these steps. Hela cells were used [41].
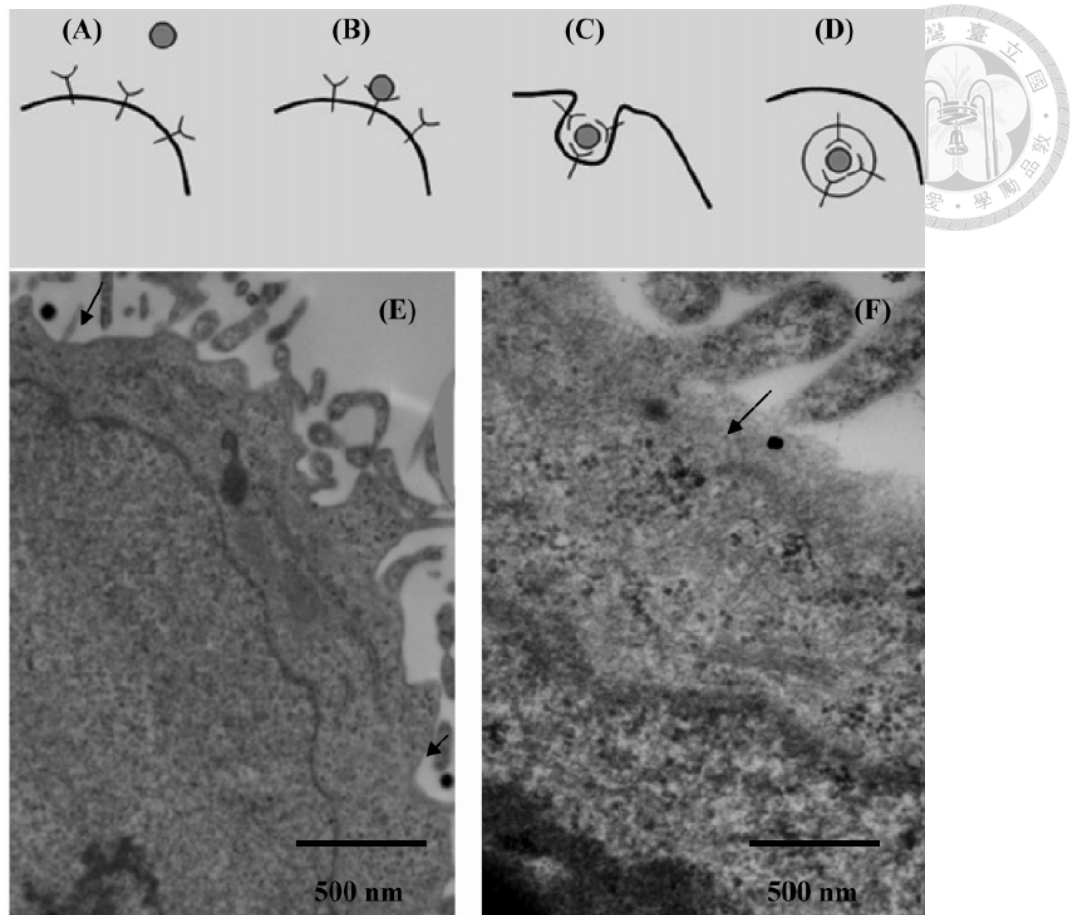
Fig. 1.14 Different stages of the cellular uptake process of _50 nm transferrin-coated Au NP. (A-D) Schematic depicting the arrival of a NP at the cell membrane, binding of the nanopartcles to surface receptors, membrane wrapping of the NP, and finally internalization into the cell, respectively. (E-F) TEM images capturing the endocytosis of nanoparticles into Hela cells [41].
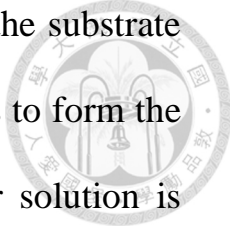
Chapter 2
Materials and Methods

2.1 Fabrication of Bio-conjugated Au Nanorings

Figures 2.1(a)-2.1(g) show the fabrication procedures of bio-conjugated Au NRI solution. In the first step, a Si nano-imprint mold is used to impress a polymer substrate for forming a nanopillar array on it. The diameter and height of the nanopillars are 180 and 100 nm, respectively. The schematic demonstration of this step and the resultant tilted SEM image of the substrate are shown in Figs. 2.2(a) and 2.3(a), respectively. Then, O_2 plasma is applied in a reactive ion etching (RIE) process to adjust the diameter and height of the nanopillars, as shown in Figs. 2.1(b) and 2.2(b) for the schematic demonstration and the resultant SEM image, respectively. In one of the implementations leading to the results to be discussed in the following, the nanopillar diameter and height are reduced to ~70 and ~80 nm, respectively. Next, an Au film of ~23 nm in thickness is deposited onto the polymer substrate to serve as the source of secondary sputtering, as depicted in Fig. 2.1(c). The secondary sputtering is implemented through a process of CHF_3 RIE under the conditions of 30 SCCM in gas flow rate, 1.3 Pa in pressure, 80 W in RF power, and 565 s in RIE duration. In this process, the Au atoms on the tops of the nanopillars are removed. Meanwhile, the Au atoms on

the substrate surface in the gap regions between nanopillars are sputtered onto the sidewalls of the nanopillars to form a ring shape, as depicted in Fig. 2.1(d). The tilted SEM image after this step is shown in Fig. 2.2(c). Then, another step of O_2 RIE is applied to remove the polymer inside the Au ring structure, i.e., the original pillar body. In this stage, the background substrate level is also lowered to form new pillars with the Au ring structures at the tops, as depicted in Fig. 2.1(e). The plan-view and tilted SEM images of the Au NRIs on substrate after this step are shown in Figs. 2.2(d) and 2.2(e), respectively. To enhance the robustness of the Au ring structure, the sample is thermally annealed at 170-180 $^{\circ}$C for 10 min. The purposes of the thermal annealing process are to avoid the breakage of Au NRI after liftoff and to enhance the overall CRD LSP resonance strength. We use the ratio of the overall LSP resonance peak level over the background level in the extinction spectrum (within the measurement range of 400-1300 nm) of an Au NRI solution at 4 as the criterion of the CRD LSP resonance strength. It is noted that RIE is a semi-physical and semi-chemical reaction process, depending on the chosen etching chemicals. With O_2 as the etching gas, RIE is essentially a chemical process and can easily etch polymers. In our operation with CHF_3, RIE mainly causes a physical process of bombarding the Au atoms to result in the effect of secondary sputtering.

Next, the bio-conjugation process is applied to the Au NRIs when

they are still attached to the substrate. In this process, first, the substrate with Au NRIs is immersed in a biolinker solution for 4 hours to form the carboxyl groups on the surface of Au NRIs. The biolinker solution is prepared by mixing a Nanothinks acid16 (5mM in ethanol, Sigma-Aldrich) solution of 30 μL with 15 mL de-ionized water. Then, the sample is rinsed in de-ionized water for several times to remove the residual biolinker. Next, the sample is immersed in a mixed solution of 100 μL (100 mM) 1-ethyl-3-[3-dimethylaminopropyl] carbodiimide hydrochloride (EDC), 25 μL (100 mM) N-hydroxysulfosuccinimide (sulfo-NHS), and 15 mL phosphate buffer saline (PBS) solution for 20 min to activate the biolinker. Then, the monoclonal anti-EGFR antibody (20 μL , 0.5 mg/mL, Anti-EGFR (26-125) mAb, Abnova) is added to the mixed solution for antibody connection. After the interaction for 22 hours, the sample is rinsed again to remove the residual antibody and other chemicals. The bio-conjugation process is schematically depicted in Fig. 2.1(f). After this process, the tilted SEM image of the on-substrate Au NRIs is shown in Fig. 2.2(f). From the SEM images of several samples at this stage, it is estimated that ~5 % of Au NRIs can be lost during the bio-conjugation process. To transfer the Au NRIs into water solution, the substrate is placed in a glass bottle with a proper amount of PBS. Sonication (NeyTech 104H with a power of 340 W for 5 min) is applied

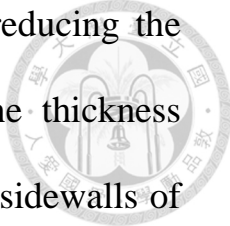until >95 % of the NRIs, which still remain on the substrate after the bio-conjugation process, are transferred into water, as depicted in Fig. 2.1(g). Figure 2.3 shows a tilted SEM image of the substrate after Au NRI liftoff with sonication. The only Au NRI remained on the substrate is indicated by the arrow. To avoid NRI aggregation in solution, PEG-Thiol (mPEG-Thiol-5000, Laysan Bio Inc., Arab, AL) is added to the NRI solution. The concentration of PEG-Thiol in the NRI solution is 1×10^{-4} M. Fig. 2.4(a) shows the SEM image of the fabricated Au NRIs when the dried-up Au NRIs are placed on a Si substrate. Figure 2.4(b) shows the photograph of Au NRI solution in a container. Its concentration is estimated to be 10^{11} per mL. The Au NRI concentration in the solution is estimated by evaluating the number of the on-substrate Au NRIs and by assuming that 90 % of the Au NRIs are transferred into the solution [35].

To confirm the surface modification procedures, the zeta potential levels under different surface modification conditions of Au NRIs are measured. First, we measure the zeta potential of pure NRIs and obtain the value is -34.51 mV. It shows there are negative charges left on the surface of NRIs during the fabrication process. After the biolinker is applied to the Au NRIs, the zeta potential is -34.55 mV. The zeta potential is basically the same because the carboxyl groups in the biolinker are also possess negative charge. Then, after antibody is applied to the Au NRIs besides the biolinker, the zeta potential becomes -23.51 mV, which is a

sign for we've successfully bio-conjugated the biolinker to the antibody. The zeta potential magnitude is reduced because the carboxyl groups of part of the biolinker are linked to the amine groups of the antibody such that the negative surface charge of the Au NRIs is decreased. Next, when the biolinker, antibody, and PEG-Thiol are applied to the Au NRIs, the zeta potential becomes -21.08 mV. If only PEG-Thiol is applied, the zeta potential becomes -17.55 mV. The above two data show that PEG-Thiol will not replace biolinker-antibody. Although the antibody can be directly linked to an Au NP without using a biolinker [57], we use the biolinker in this work for connecting the antibody and the Au NRIs to assure the strong bonding between them. Our zeta potential measurements confirm that the function of the biolinker works.

Consider the cell uptake efficiency is better for small NPs, we attempt to fabricate NRIs with CRD LSP resonance wavelength near 1064 nm, which is the output wavelength of our CW laser, as small as possible to promote the amount of NRIs taken up by SAS cells. In chapter 1.3, we've talked about the characteristics of Au NRI. In order to fabricate smaller NRIs and make the resonance wavelength remain near 1064 nm at the same time, we have to reduce the diameter, which leads to blue shift, the height and the thickness, both which leads to red shift. In order to reduce the diameter, we have to increase the first CHF_3-O_2 RIE process time to ~220 s and control the diameter in the range from 65 nm

to 70 nm. Then, we attempt to decrease the thickness by reducing the thickness of deposited Au film to 21~23 nm. Because the thickness cannot increase further after all Au atoms are sputtered onto sidewalls of polymer nanorods, reducing the thickness of the deposited Au film can effectively reduce the thickness of NRIs. Finally, we deal with height by increasing the second CHF_3 RIE process time. With the second CHF_3 RIE process, the Au atoms attached to the sidewall of a polymer nanorod can be removed from the top to make the fabricated Au NRI shorter (smaller h), as schematically shown in Fig. 2.5. Because the stability of RIE process is not perfectly good, SEM is used to check if the wanted dimensions of diameter, thickness, and height are achieved. As a result, NRIs with diameter near 105 nm, thickness near 18 nm, and height near 75 nm perform LSP resonance near 1065 nm. Figure 2.6 shows six examples of NRIs with similar geometry diameters. From (a) to (f) the diameter, thickness, height (represented by D, d, h) are (a): (102 nm,18 nm,73 nm), (108 nm,20 nm,80 nm), (100 nm,16 nm,75 nm), (109 nm,19 nm,80 nm), (100 nm,20 nm,70 nm), (108 nm,20 nm,70 nm). All of them have similar CRD LSP resonance wavelength near 1065 nm as in Fig. 2.7.

2.2 SAS Cell Culture

SAS cells (see Fig. 2.8) are donated by Yih-Chih Hsu's laboratory of

Chung Yuan Christian University. It is a poorly differentiated human squamous cell carcinoma line, cultured in DMEM/F-12 medium containing 10% FBS, 400 ng/ml hydrocortisone, 1% sodium bicarbonate and 1% antibiotic in culture flasks in humidified 5% CO, at 37°C [59-61].
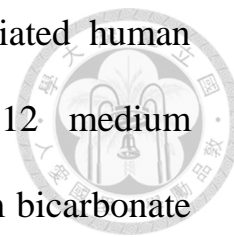
The cell inactivation experiment is conducted with 4×10^5 SAS cells seeded on a 24-well cell culture plate for 12 hours. Then, both bio-conjugated/non-bio-conjugated NRIs are applied for the durations of 8, 10, 12, 16, 20, and 24 hours, respectively. Then, the cell inactivation experiment is conducted. After SAS cells are trypsinized for ICP-MS analysis, we count the number of cell on the cell culture plate for analyzing the number of NRI per cell.

2.3   Inductively   Coupled   Plasma   Mass Spectrometer (ICP-MS) Analysis

In our experiment, we need to measure the amounts of internalized, adsorbed, and non-interacted Au NRIs. For this purpose, we use inductively coupled plasma mass spectrometry (ICP-MS) for Au quantization. The ICP-MS measurement is performed at the Instrumentation Center at National Tsing Hua University. Inductively coupled plasma mass spectrometry (ICP-MS, see Fig. 2.9) is a type of mass spectrometry, which is designed to measure metals and several

non-metals at a concentration as low as one part per 10^{12}. This kind of precision is achieved by ionizing the sample with inductively coupled plasma and then using a mass spectrometer to separate and quantify those ions. Because the content of Au contained in a sample is in the order of 10^{-9} μg/ml, highly-sensitive ICP-MS is needed to measure the Au content. Before measuring the concentration, we have to dissolve Au NRIs with aqua regia for uniform distribution of the solution.
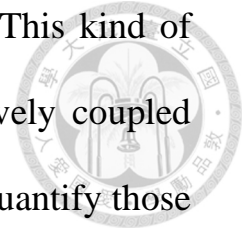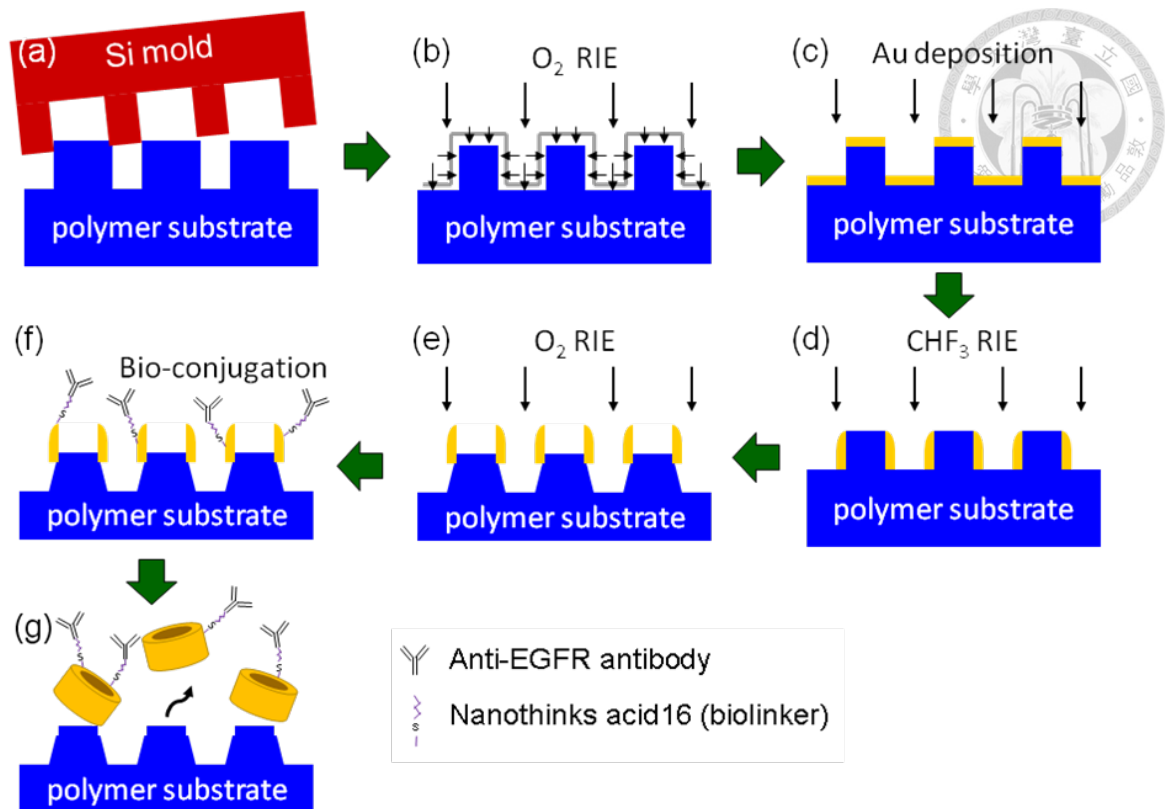
Fig. 2.1 Fabrication procedures of bio-conjugated Au NRI solution. (a): Nano-imprint step to prepare the polymer substrate with nanorods; (b): First O_2 RIE step to modify the geometry of the polymer nanorods; (c): Au deposition step. (d): CHF_3 RIE step for secondary sputtering of Au to form the ring shape. (e): Second O_2 RIE step to remove the polymer nanorods and lower the substrate surface. (f): Bio-conjugation step. (g): Sonication step to transfer Au NRIs into water solution.
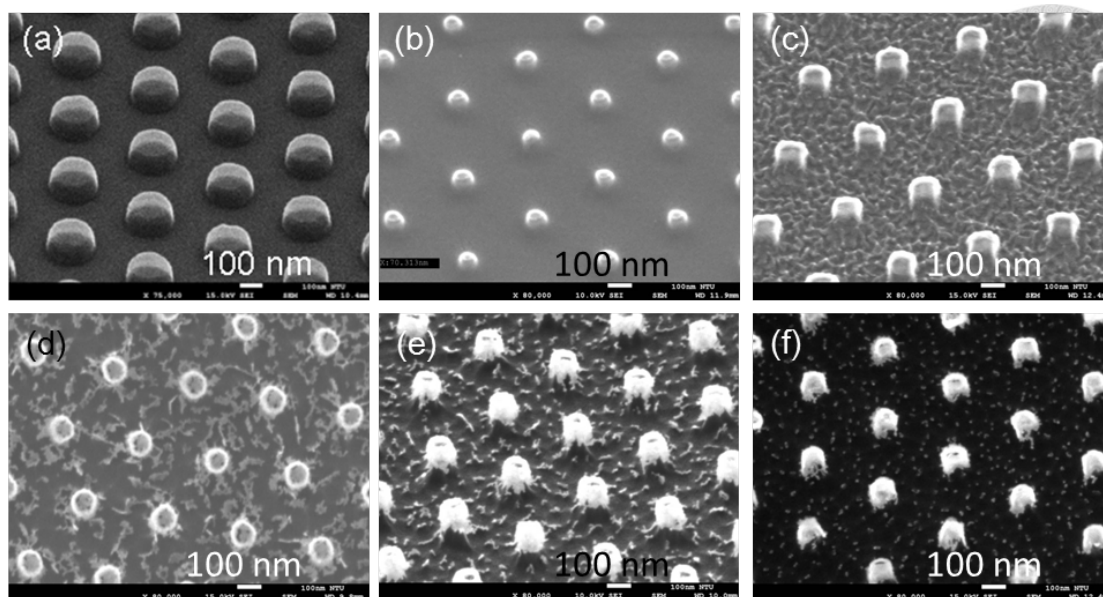
Fig. 2.2 SEM images on the substrate showing the results after various fabrication steps. (a): After the nano-imprint step. (b): After the first O_2 RIE step. (c): After the Au deposition and CHF_3 RIE steps; (d) and (e): After the second O_2 RIE step (plan-view and tilted-view, respectively). (f): After the bio-conjugation process.
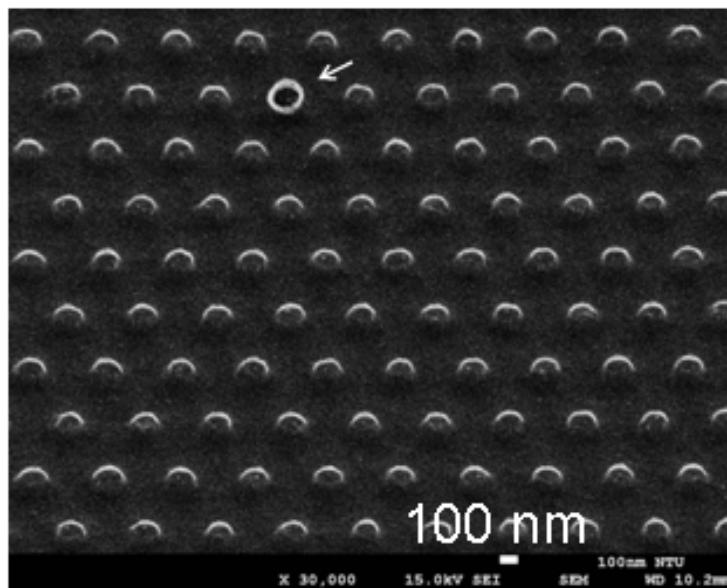
Fig. 2.3 Tilted SEM image of the substrate after Au NRI liftoff with sonication. The Au NRI remained on the substrate is indicated by the arrow.
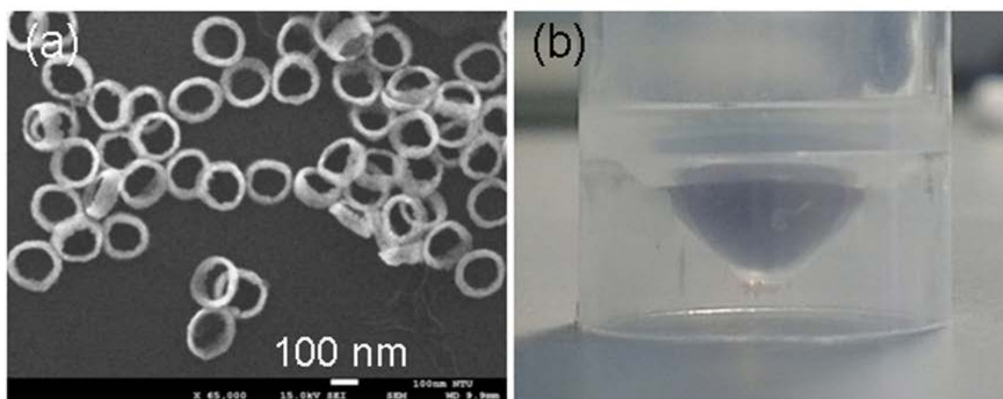

Fig. 2.4 (a): SEM image of the fabricated Au NRIs taken when the dried-up Au NRIs are placed on a Si substrate. (b): Photograph of an Au NRI solution in a container.
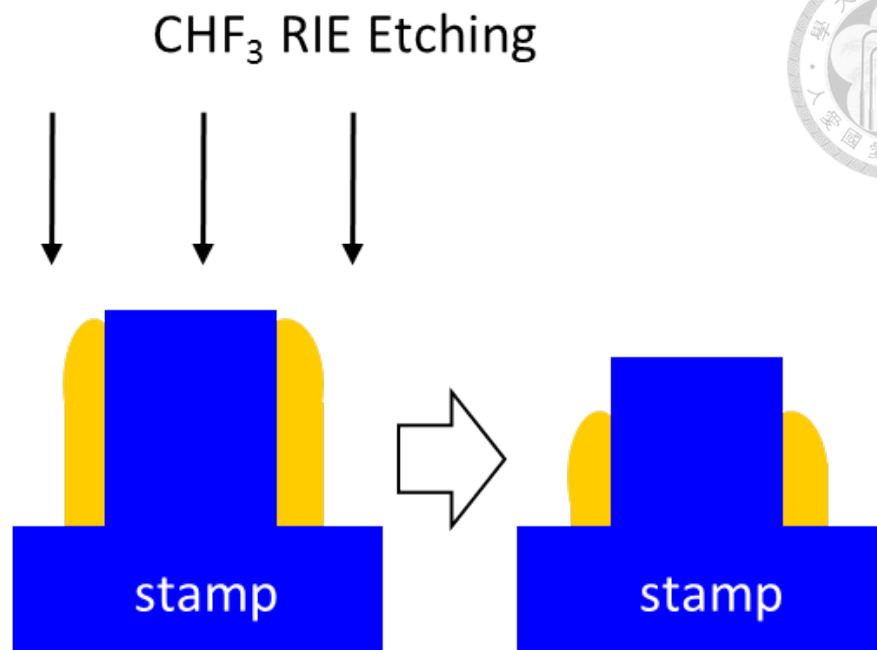
Fig. 2.5: Schematic drawing to show the reduction of ring height in the second CHF_3 RIE process.
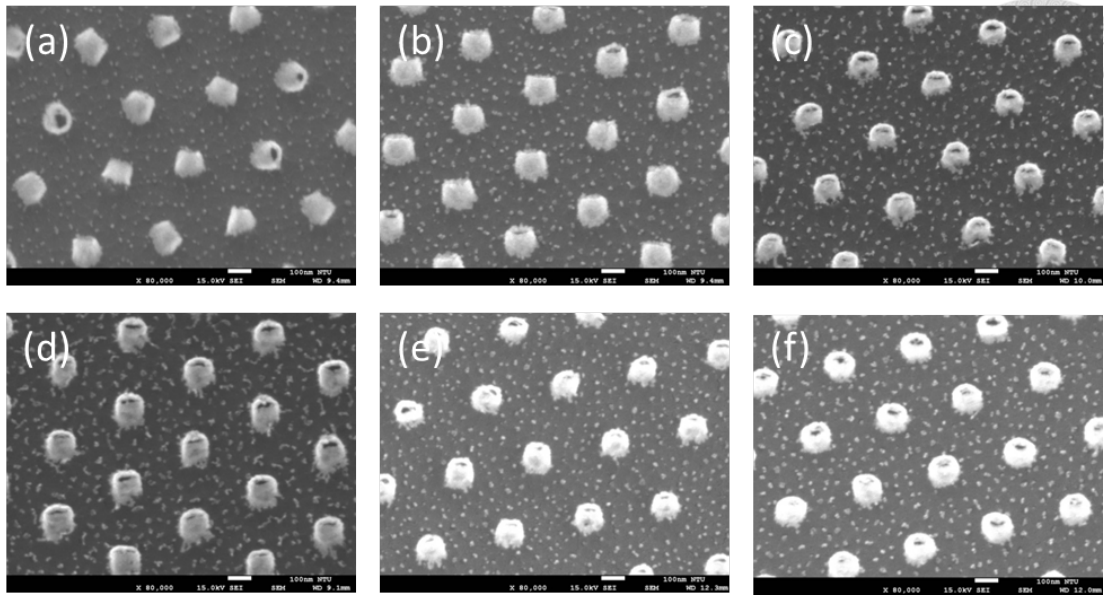
Fig. 2.6 (a)-(f) are tilted SEM images of NRI arrays on polymer substrate (samples I-IV, respectively). The followings are three geometry parameters (diameter, D, thickness, d, and height, h) of each sample. (a)D=102 nm, d=18 nm, h=73 nm (b) D=108 nm , d=20 nm, h=80 nm (c)D=100 nm, d=16 nm, h=75 nm (d) D=109 nm, d=19 nm, h=80 nm (e) D=100 nm, d=20 nm, h=70 nm (f) D=108 nm, d=20 nm, h=70 nm, all of them are similar in these dimensions.
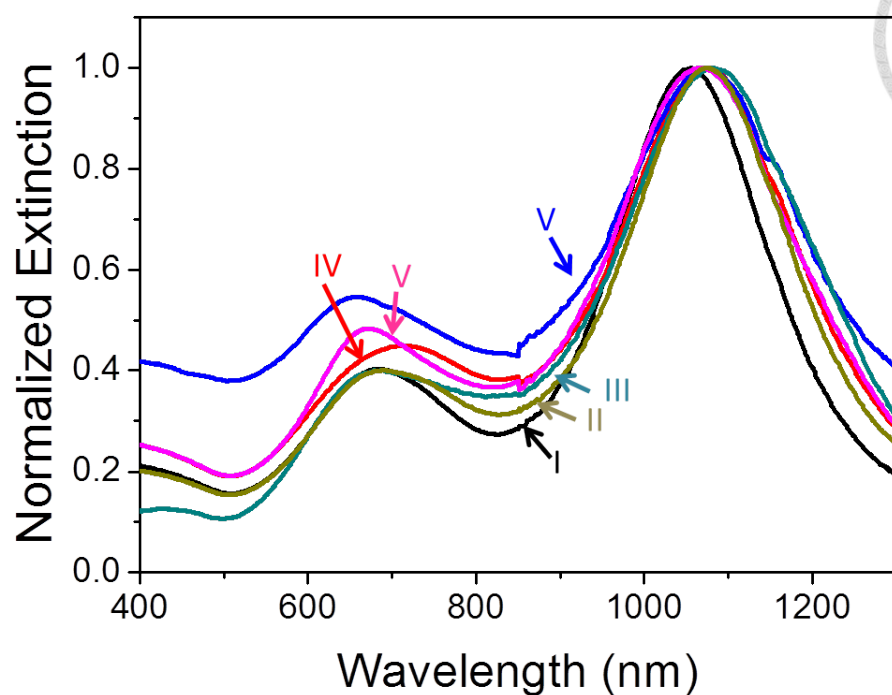
Fig. 2.7 Normalized extinction spectrums of I-IV sample are illustrated in this figure. With similar diameters, thicknesses, and heights, the CRD LSP resonance wavelength of each sample are pretty close.
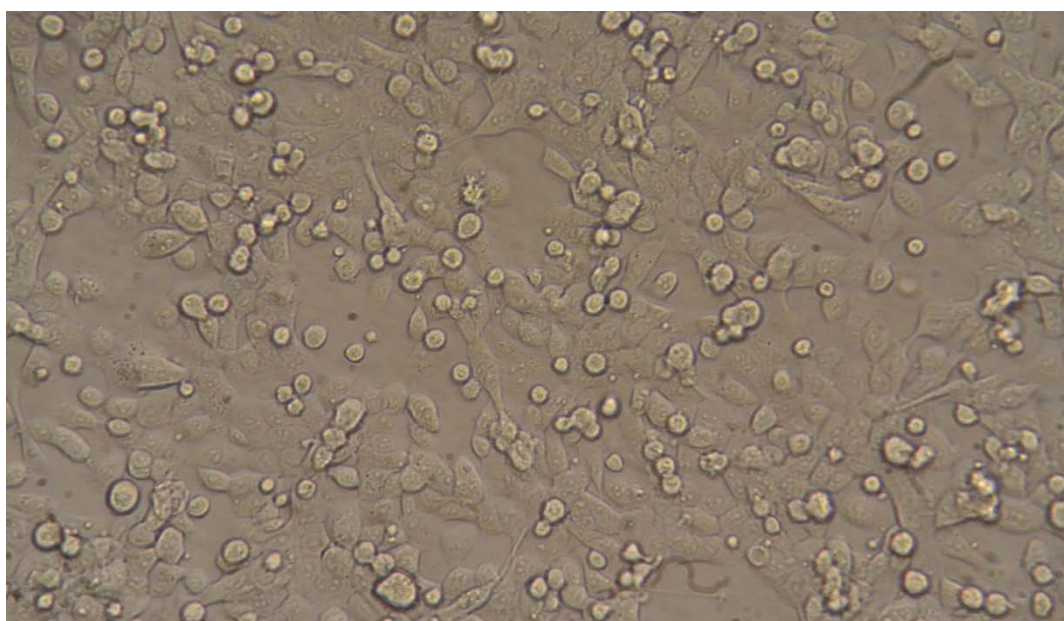

Fig. 2.8 SAS cells in cell culture medium.

Fig. 2.9 Inductively Coupled Plasma Mass Spectrometer (ICP-MS).

Chapter 3
Cell Inactivation by Localized Surface Plasmon-induced Photothermal Effect

3.1 Experimental Procedures

The insert of Fig. 3.1 shows the SEM image of the used Au NRIs before liftoff. Figure 3.1 shows the normalized extinction spectrum of the Au NRIs in PBS with PBS as the base line of transmission measurement. The average outer diameter, thickness, and height of the Au NRIs are 102, 18, and 66 nm, respectively. Two Au NRI solution samples are prepared, including the one with antibody (NRI-AB) and another without antibody (NRI-control). The Au NRI concentrations of the NRI-AB and NRI-control solutions are $(1.51\pm0.12)\times10^{10}$ and $(1.74\pm0.18)\times10^{10}$ cm^{-3}, respectively. The zeta potentials of the NRI-AB and NRI-control are -21.1 and -17.6 mV, respectively, indicating the effective antibody linkage. In Fig. 3.1, one can see that the major LSP resonance induced extinction peak is located at 1058 nm, as indicated by the vertical dashed line. The arrow next to the dashed line marks the wavelength of the excitation laser for cancer cell inactivation at 1065 nm. The extinction ratio of the peak with respect to the minimum level around 500 nm is as large as 5.42, indicating the strong cross-ring LSP resonance around 1058 nm.

Figure 3.2 shows the viability of the used cancer cell (SAS oral cancer cell) when it is incubated with Au NRI-AB and NRI-control for different incubation times (8, 12, and 24 hrs). The statistics are obtained based on the cell incubation of 24-well culture plate. From Fig. 3.2, one can see that either Au NRI-AB or NRI-control is essentially non-toxic to the used cancer cells. In the study, we will use KI/I_2 solution for etching the absorbed Au NRIs on cell membrane (not internalized yet) without significantly damage the cells. Figure 3.3 shows the normalized extinction spectra of Au NRI-AB solution before and after adding a KI/I_2 solution (0.268 mM for KI and 0.088 mM for I_2) for different durations. The extinction spectrum of the Au NRI solution in Fig. 3.1 is repeated here and labeled by "Before etching". The extinction spectra after adding the KI/I_2 solution in Fig. 3.3 are obtained by using the same KI/I_2 solution as the measurement base line. Here, one can see that after adding KI/I_2 to the Au NRI solution, the major and minor spectral peaks red- and blue-shifts, respectively, due to the increase of the refractive index after KI/I_2 is added. After the addition of KI/I_2, both the major and minor peaks diminish with time as the Au NRIs are dissolved. Also, the major and minor spectral peaks continue red- and blue-shifting, respectively, due to the continuing increase of solution refractive index caused by the increase of Au ion concentration after the Au NRIs are etched. The extinction spectra after KI/I_2 is added are measured every 3 min. One can see that

after 60 min etching, the major Au NRI features disappear. The optimized etching time of KI/I$_2$ also relies on the cell viability in KI/I$_2$ solution. Figure 3.4 shows such data at different etching durations. With 60 min in etching duration, 96.6 % cells can still survive. Therefore, we choose 60 min as the optimized KI/I$_2$ etching duration for almost completely etching the Au NRIs outside cells and maintain reasonably high cell viability.

Figures 3.5(a)-3.5(c) schematically show the different laser illumination and cancer inactivation conditions in this study. As demonstrated in Fig. 3.5(a), after the designed incubation time upon the application of Au NRIs to cancer cell wells, the cancer cell is illuminated by the laser from the bottom. This condition is referred to as "Pre-washout", under which the Au NRIs can be internalized into the cells, adsorbed on the cells, suspended in the cell culture medium, and settled at the bottom of the solution. Then, as demonstrated in Fig. 3.5(b), the cancer cell is washed five times with PBS after the designed incubation time for another laser illumination experiment. This is the condition of "Post-washout", under which the Au NRIs suspended in the cell culture medium and settled at the bottom of the solution are removed. Only those either internalized or adsorbed by cancer cells are kept for observing the effect of photothermal inactivation of cancer cell. The Au content in the flushed solution is measured with ICP-MS for evaluating the Au NRI percentage neither internalized nor adsorbed. Next, as

demonstrated in Fig. 3.5(c), the KI/I_2 solution is added to the cell well for etching the Au NRIs adsorbed on the membrane of cells after the designed incubation time. After one-hour KI/I_2 etching, the cell is washed again to flush the resolved Au. This is the condition of "After-etching", under which only the Au NRIs internalized by cells are kept in the cell for inducing the photothermal effect upon laser illumination. The Au content of the flushed solution of resolved Au is also measured with ICP-MS for evaluating the percentage of Au NRI adsorbed on the membrane of the cells. After the laser illumination experiment, cells in the well, including the internalized Au NRIs, are measured with ICP-MS for evaluating the percentage of Au NRI internalized. Given the cell number per well, the ICP-MS data can lead to the results of average NRI numbers per cell internalized and adsorbed.

Figure 3.6 shows the optical images of the cell under various conditions of incubation time and washout/etching process when NRI-AB is applied to the cell. Here, the dark spots correspond to the distribution of Au NRIs. Under the condition of post-washout, the NRI concentration in the cell culture medium is reduced, when compared with that under the condition of pre-washout. After etching, the NRI concentration in the cell is further decreased under each condition of incubation time. Among the conditions of different incubation times, the Au NRI concentrations are about the same in the situation of pre-washout. Also, a longer incubation

time leads to a higher Au NRI concentration under either condition of post-washout or after-etching, indicating that with a longer incubation time, more Au NRIs are either adsorbed or internalized. Figure 3.7 shows the optical images of the cell under various conditions of incubation time and washout/etching process when NRI-control is applied to the cell. The variation trends of the images among different conditions are similar to those in Fig. 3.6. However, the image contrasts are not high enough for clearly observing the variation trends. The low image contrasts here can be attributed to the lower aggregation of Au NRI-control. With the linkage of only PEG in the NRI-control, the aggregation of Au NRIs is weaker, when compared with the NRI-AB, which links to both PEG and antibody. The aggregated Au NRIs can be more easily observed in an optical image. The NRIs-control can be more aggregated after they are internalized into the cells. Therefore, as shown in Fig. 3.7, the dark spots can be more easily observed in the cases of long incubation times.

3.2 Experimental Results

Laser illumination experiments are undertaken under all the 18 conditions shown in either Fig. 3.6 or 3.7. Under each condition, the microscopic images of the cell in a well around four laser illumination spots are taken after it is stained by trypan blue for showing the cell
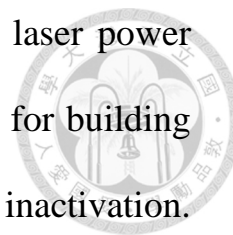
viability after the LSP-induced photothermal process. In each case, four laser power levels of 230, 200, 200, and 180 mW are used for the four collimated illuminations onto the same well. Cell inactivation is expected to be observed in a circular area around the center of the circular laser spot. The radius of the inactivation circular area is determined by the illuminated laser power and Au NRI concentration in the cell culture meduim. Figures 3.8(a)-3.8(l) and 3.9(a)-3.9(l) demonstrate two typical sets of such microscopic images. In Figs. 3.8(a)-3.8(d), we show the images with the laser powers of 230, 200, 200, and 180 mW, respectively, under the condition of pre-washout when the NRI-AB solution is applied to the cell wells and the incubation time is 16 hrs. In Figs. 3.8(e)-3.8(h) and 3.8(i)-3.8(l), we show the corresponding images under the conditions of post-washout and after-etching, respectively. Figures 3.9(a)-3.9(l) show the microscopic images corresponding to Figs. 3.8(a)-3.8(l) when the NRI-control solution is applied to the cell wells and the incubation time is 12 hrs. Here, the cancer cells within the blue areas are inactivated though the LSP-induced photothermal effect. The dark spots at almost the centers of the circular blue areas are caused by the burning of well bottom due to the settlement of Au NRIs for producing hot spots there under laser illumination. One can see that with a higher laser power level, the blue area becomes larger, indicating the larger radius of laser illumination spot to reach the threshold intensity for cancer cell inactivation. By comparing
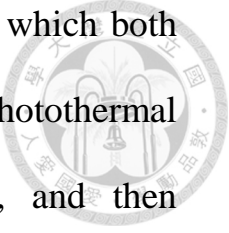
Figs. 3.8(a)-3.8(l) with 3.9(a)-3.9(l), one can see that under the condition of pre-washout, the blue areas of cell inactivation with Au NRI-AB are generally quite close to those of the corresponding cases with NRI-control since the applied Au NRI concentrations of the two Au NRI samples of different surface modifications are not so different. However, under the conditions of post-washout and after-etching, the blue areas of cell inactivation with Au NRI-control are generally smaller than those with NRI-AB, indicating that the percentages of Au NRI adsorbed and internalized are relatively lower in the case without linking the antibody to the Au NRI.

Dashed lines are drawn in the microscopic images to circle the blue areas in Figs. 3.8(a)-3.8(l) and 3.9(a)-3.9(l) for evaluating the threshold local laser intensity of cancer cell inactivation. The radius of a drawn circle is denoted as r_{th}. By assuming a Gaussian laser beam with the intensity profile as $I(r) = I_0\exp(-r^2/r_0^2)$, the total laser power is $P = \pi I_0 r_0^2$. Here, I_0 is the peak intensity, r stands for the radius, and r_0 represents the beam size. At the beam radius of the threshold intensity for cell inactivation, $I_{th} = I_0 \exp(-r_{th}^2/r_0^2)$ or $I_{th} = (P/\pi r_0^2) \exp(-r_{th}^2/r_0^2)$. (1) Because I_{th} is a constant for a particular Au NRI sample, by using the experimental data (P and r_{th}) of two laser power levels, we can solve for r_0 and I_{th} from equation (1). Therefore, the four sets of data from the four microscopic images in the same row of either Figs. 3.8(a)-3.8(l) or Figs.

3.9(a)-3.9(l) can lead to five combinations of two different laser power levels. Each combination can result in a set of (r_0, I_{th}) value for building up the statistics of laser threshold in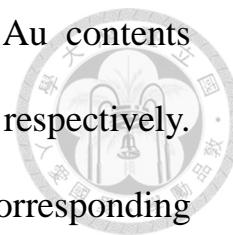tensity of cancer cell inactivation. The similar results of r_0 in these five combinations provide us with the confidence for the reasonable calibration of the threshold intensity of cancer cell inactivation. Based on the procedures described above, we can obtain the average and standard deviation of the threshold laser intensity under any condition of pre-washout, post-washout, or after-etching for each case of incubation time when either NRI-AB or NRI-control is applied to the cell. Such results are summarized in Figs. 3.10 and 3.11 for the cases of NRI-AB and NRI-control, respectively. In either Fig. 3.10 or 3.11, one can see that the threshold laser intensities under the condition of pre-washout are generally lower than those under the conditions of post-washout and after-etching. Such results are attributed to the strong heating effect of those Au NRIs suspended and settled in the cell culture medium. The induced high temperature in the illuminated spot can inactivate the cells. Because the applied Au NRI concentrations to the cell culture medium of the cases of NRI-AB and NRI-control are not so different, the threshold laser intensities of the two cases under the condition of pre-washout are about the same regardless the incubation time. However, the variation trends of threshold laser intensity under the conditions of post-washout and after-etching are quite different. In the

case of NRI-AB under the condition of post-washout, under which both the adsorbed and internalized Au NRIs contribute to the photothermal effect, the threshold laser intensity decreases, increases, and then decreases again with incubation time. Then, under the condition of after-etching, the threshold laser intensity decreases with incubation time, indicating the increasing amount of Au NRI internalized. Since the threshold laser intensities under the condition of post-washout are generally lower than those under the condition of after-etching, we can speculate that the photothermal effect due to the adsorbed Au NRIs is quite effective in cell inactivation. This issue will be further discussed later. In the case of NRI-control, the result of 8-hr incubation under the condition of post-washout and those of 8- and 12-hr incubation times under the condition of after-etching are missing because no cell inactivation feature can be found around the laser illumination spot, indicating that in these situations, the adsorbed or internalized Au NRIs are too few to achieve strong enough photothermal effect for cell inactivation. The aforementioned missing data and the significantly higher threshold laser intensities with 10-hr incubation time under the condition of post-washout and with12-hr incubation time under the condition of after-etching imply that when the incubation time is not long enough, the amounts of adsorbed and internalized Au NRIs are small.

From the ICP-MS measurement results of the flushed solution after

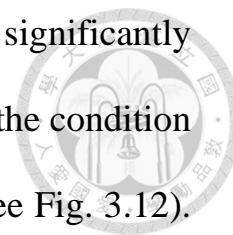KI/I$_2$ etching and the remained cells, we can obtain the Au contents (weights) adsorbed on the cell membrane and internalized, respectively. From the obtained data of au weights, we can evaluate the corresponding Au NRI numbers. Given the cell number per well with a cell counter, we can obtain the average NRI numbers per cell adsorbed and internalized. Figures 3.12 and 3.13 show the average NRI numbers per cell adsorbed and internalized, and their summation (total uptake NRI) with different incubation times when NRI-AB and NRI-control, respectively, are used for cell inactivation experiments. We can see that either adsorbed or internalized NRI-AB number per cell is significantly higher, when compared with the corresponding value of NRI-control, indicating the function of the antibody. In Fig. 3.12, one can see that the internalized NRI-AB number per cell increases with incubation time. However, the adsorbed NRI-AB number per cell increases when the incubation time increases from 8 to 12 hours and then decreases with incubation time. Such a variation trend is attributed to the increased internalization speed after 12 hours in incubation time. It is noted that before internalization, NRIs are first adsorbed onto cell membrane. With the increasing speed of internalization, the number of NRIs remaining on cell membrane, which is defined as the adsorbed NRI number in Fig. 3.12 or 3.13, is reduced. As shown in Fig. 3.13, the increase of internalization speed of NRI-control starts later at 20 hrs in incubation time. From the ICP-MS

measurement results of the flushed solution in the washout stage, we can obtain the Au content not adsorbed or internalized and hence the total applied Au content to the cell at the beginning (by summing up this Au content with those adsorbed and internalized). Figure 3.14 shows the percentages of the adsorbed, internalized, and total uptake NRIs (the summation of the adsorbed and internalized NRIs) out of the applied NRIs for both cases of NRI-AB and NRI-control. Here, we can see that up to 33 % applied NRI-AB can be taken up by the cancer cell, either adsorbed or internalized, when the incubation time is 24 hrs. Also, up to 12.5 % applied NRI-control can be taken up by the cancer cells when the incubation time is 24 hrs.
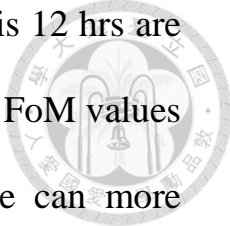
3.3 Discussions

The decreasing trend of the threshold laser intensity for cancer cell inactivation with incubation time under the condition of after-etching shown in Fig. 3.10 is consistent with the increasing internalized NRI-AB number per cell with incubation time shown in Fig. 3.12. Under the condition of post-washout, as shown in Fig. 3.10, except the case of 24 hours in incubation time, the threshold laser intensities with other incubation times are lower than the corresponding values under the condition of after-etching even though their total uptake NRI-AB

numbers per cell under the condition of post-washout are significantly smaller than the internalized NRI-AB number per cell under the condition of after-etching in the case of 24 hours in incubation time (see Fig. 3.12). This result can be attributed to the relatively more effective cell inactivation of the adsorbed NRIs, when compared with the internalized NRIs. This attribution can be particularly supported by the relatively larger adsorbed NRI number per cell (see Fig. 3.12) and the relatively lower threshold laser intensity (see Fig. 3.10) for cell inactivation when the incubation time is 12 hours. The decreasing and then increasing trends of threshold laser intensity under the condition of post-washout when the incubation time is increased from 8 through 20 hours, as shown in Fig. 3.10, are consistent with the variation trend of the adsorbed NRI-AB number per cell shown in Fig. 3.12. When the incubation time is 24 hours, the internalized NRI-AB number per cell is tremendously increased such that the threshold laser intensity is decreased. Since the threshold laser intensity is expected to decrease with increasing uptake NRI number per cell, we can define a figure of merit (FoM) of cancer cell inactivation as the multiplication of the threshold laser intensity and total uptake or internalized NRI number per cell. A lower FoM implies a more effective cancer cell inactivation process. For instance, the FoMs of the internalized and total uptake NRIs when the incubation time is 24 hrs are 16477 and 16994 W/cm^2, respectively. Meanwhile, the FoMs of the

internalized and total uptake NRIs when the incubation time is 12 hrs are 8912 and 5972 W/cm^2, respectively. The comparison of those FoM values again indicates that Au NRIs remaining on cell membrane can more effectively inactivate cancer cell. For maximizing the Au NRI number remaining on cell membrane (without internalization) for minimizing the threshold laser intensity, the incubation time cannot be too long. Under the current experimental condition, 12 hrs can be close to the optimized incubation time. The results with NRI-control are similar. In this situation, the maximum adsorbed NRI-control number per cell is observed when the incubation time is 20 hrs. Under this condition, the obtained threshold laser intensity is the smallest (see Fig. 3.11) even though the total uptake NRI number per cell (1240) is significantly smaller than the internalized NRI number per cell (1909) in the case of 24 hrs in incubation time (see Fig. 3.13). The FoMs of the internalized and total uptake NRIs when the incubation time is 24 hrs are 15291 and 15106 W/cm^2, respectively. Meanwhile, the FoMs of the internalized and total uptake NRIs when the incubation time is 20 hrs are 9427 and 5171 W/cm^2, respectively. Again, the NRIs remaining on cell membrane can cause more effective cancer cell inactivation with NRI-control. However, with NRI-control, the optimized incubation time is close to 20 hrs. Without linking antibody, the required incubation time is longer for effective cell uptake and inactivation.
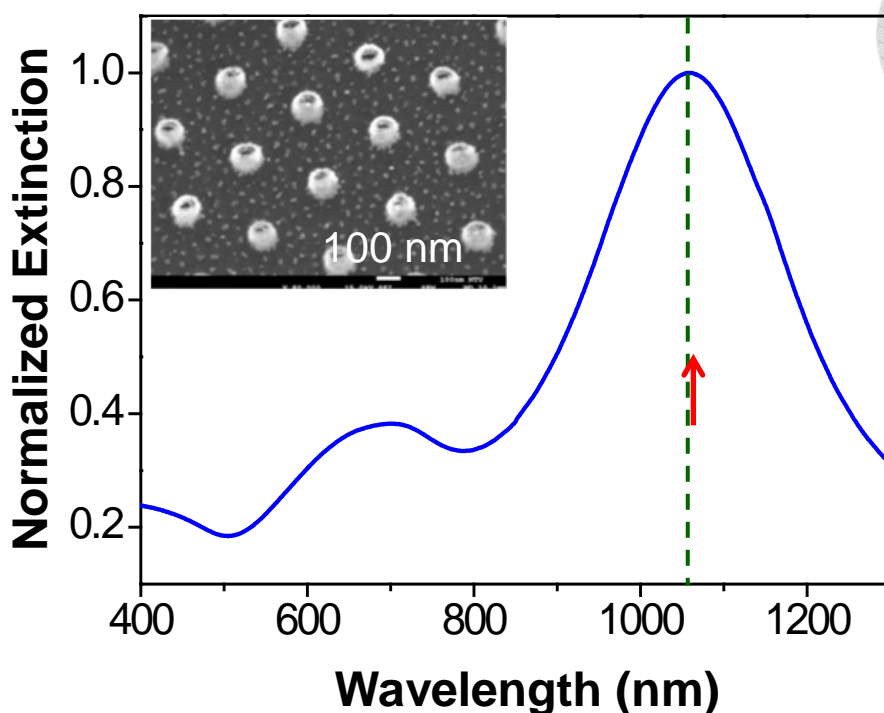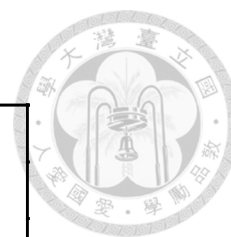
Fig. 3.1 Normalized extinction spectrum of the used Au NRIs in PBS with PBS as the base line of transmission measurement. The insert shows the SEM image of the used Au NRIs before liftoff. The major LSP resonance induced extinction peak is located at 1058 nm, as indicated by the vertical dashed line. The arrow next to the dashed line marks the wavelength of the excitation laser for cancer cell inactivation at 1065 nm.
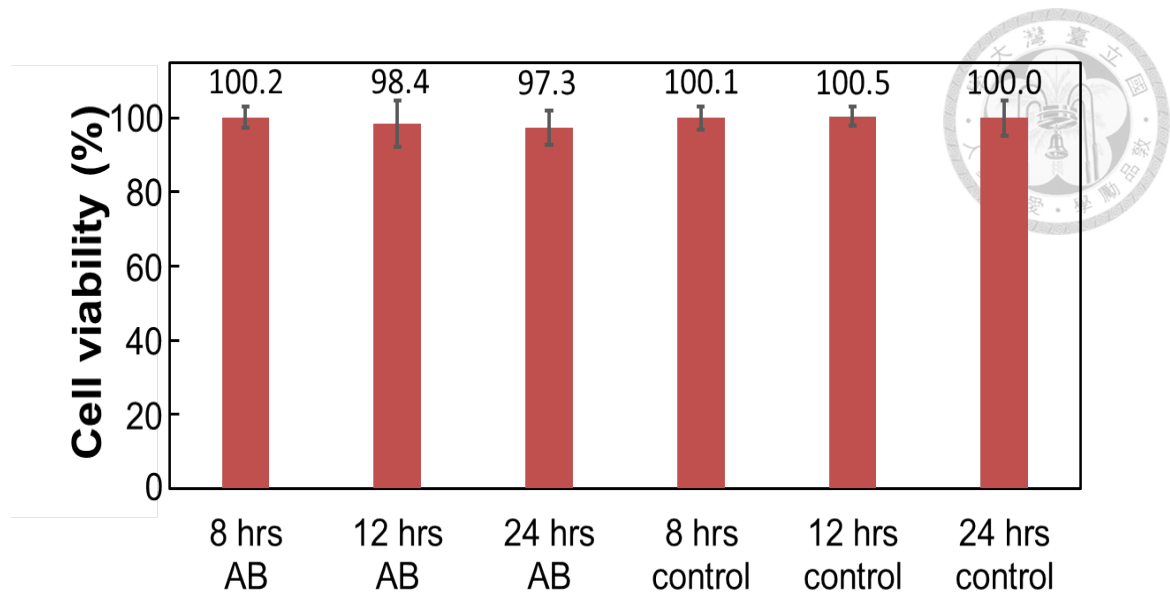
Fig. 3.2 Viability of the used cancer cell (SAS oral cancer cell) when it is incubated with Au NRI-AB and NRI-control for different incubation times (8, 12, and 24 hrs).
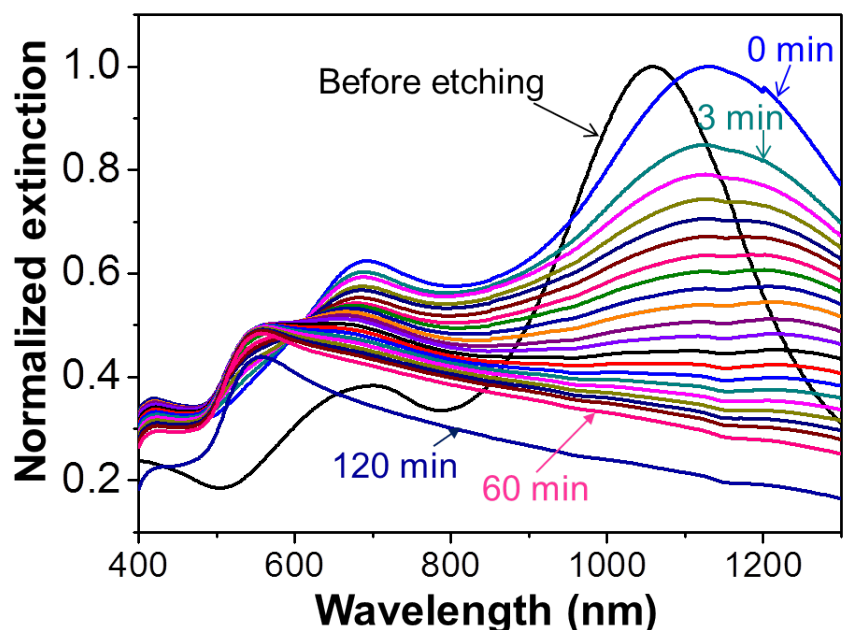
Fig. 3.3 Normalized extinction spectra of Au NRI-AB solution before and

after adding a KI/I$_2$ solution for different durations.
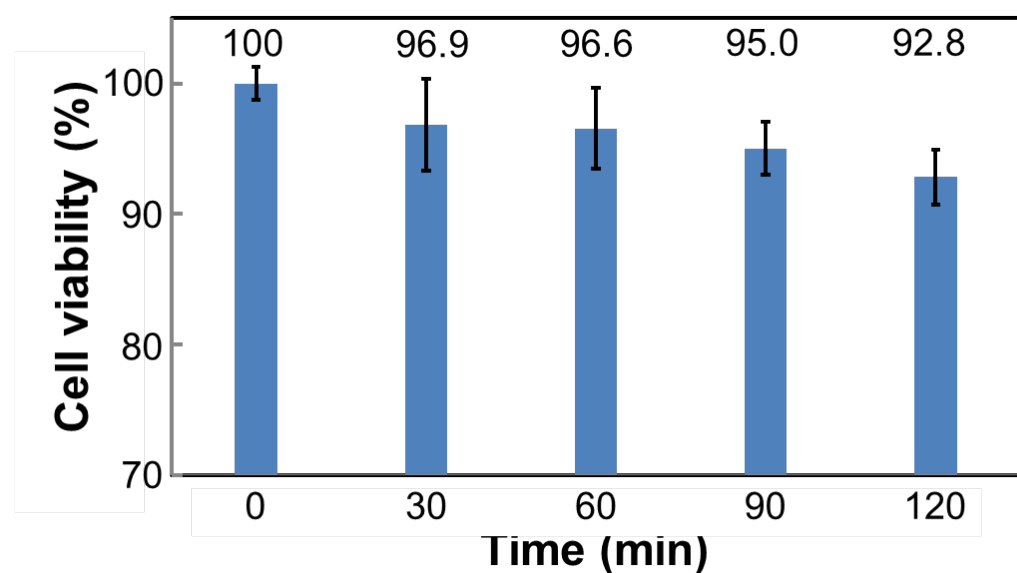
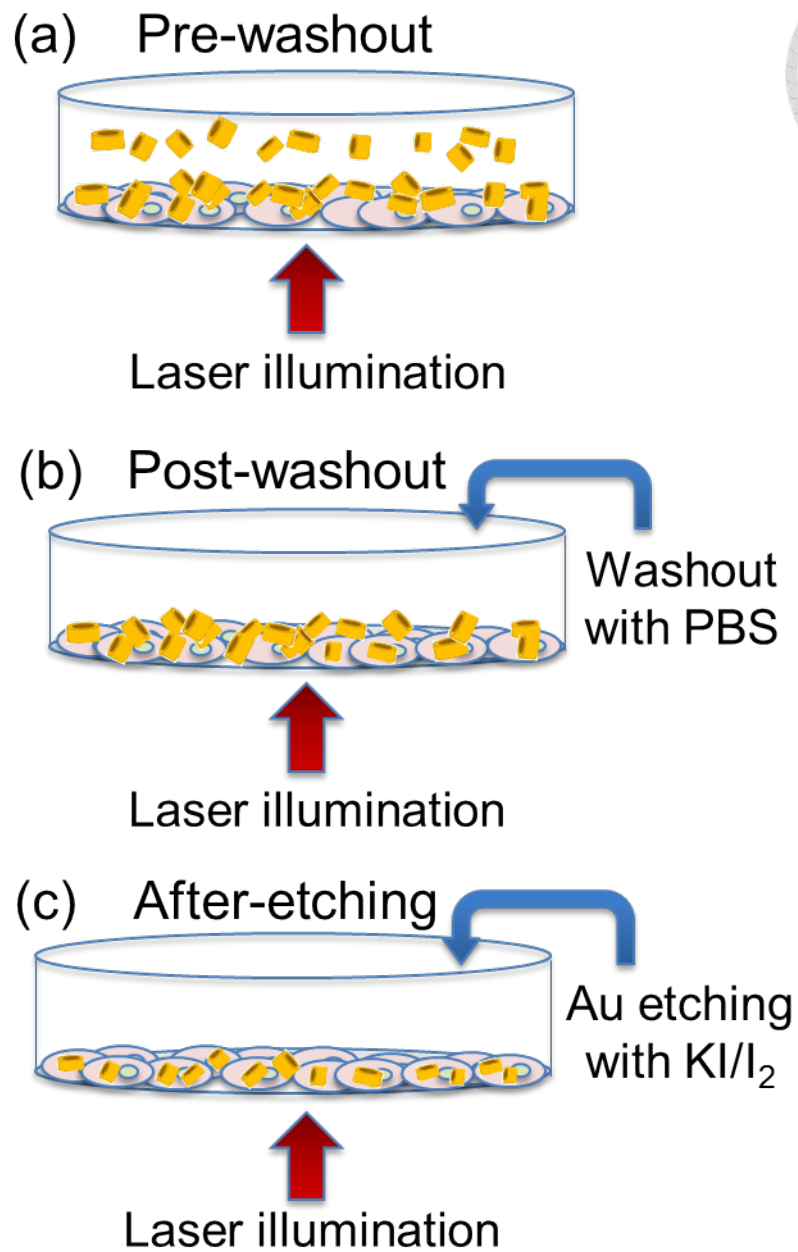Fig. 3.4 Cell viability at different KI/I$_2$ etching durations.

Fig. 3.5 (a)-(c): Schematic demonstrations of the different laser illumination and cancer inactivation conditions in this study.
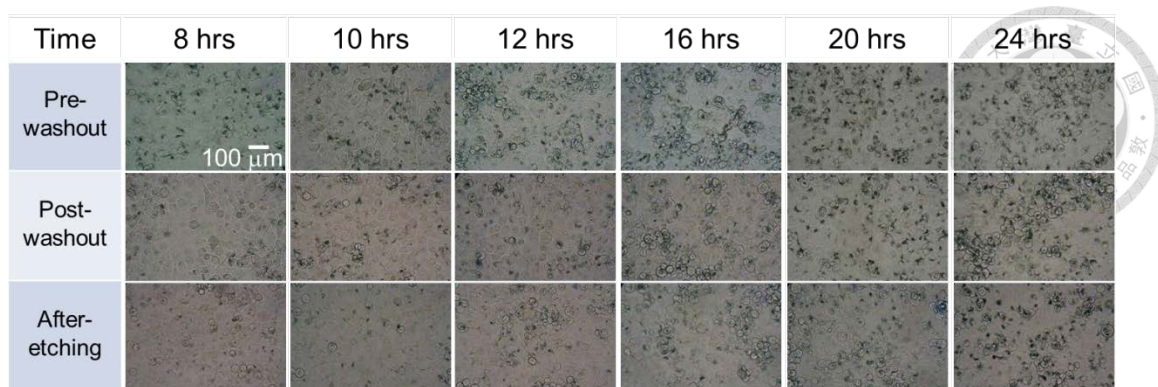
Fig. 3.6 Optical images of the cell under various conditions of incubation time and washout/etching process when NRI-AB is applied to the cell.
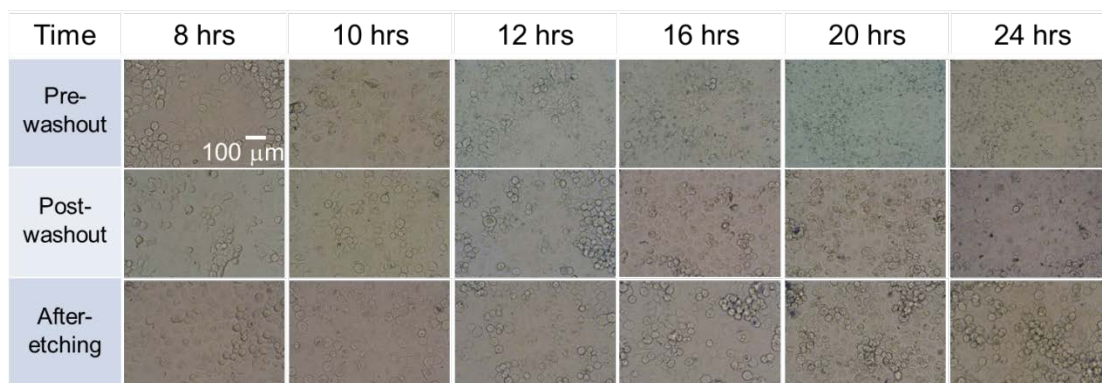

Fig. 3.7 Optical images of the cell under various conditions of incubation time and washout/etching process when NRI-control is applied to the cell.
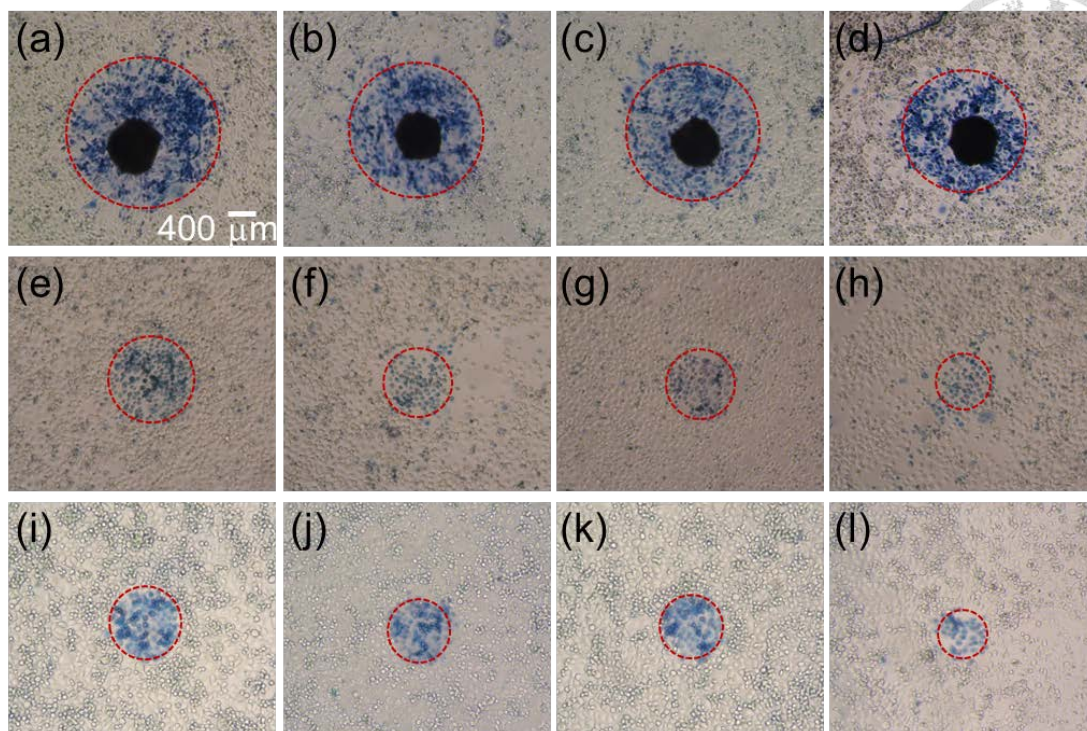
Fig. 3.8 (a)-(d): Microscopic images with the laser powers of 230, 200, 200, and 180 mW, respectively, under the condition of pre-washout when the NRI-AB solution is applied to the cell wells and the incubation time is 16 hrs. (e)-(h) and (i)-(l): Corresponding microscopic images under the conditions of post-washout and after-etching, respectively.
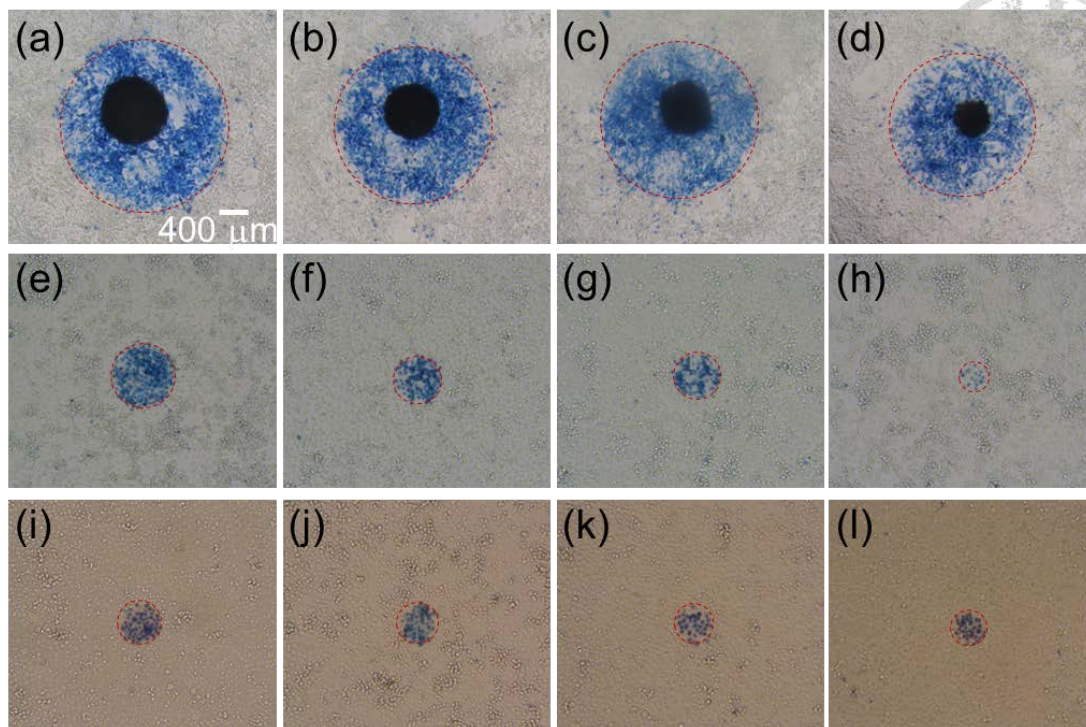
Fig. 3.9 (a)-(d): Microscopic images with the laser powers of 230, 200, 200, and 180 mW, respectively, under the condition of pre-washout when the NRI-control solution is applied to the cell wells and the incubation time is 12 hrs. (e)-(h) and (i)-(l): Corresponding microscopic images under the conditions of post-washout and after-etching, respectively.
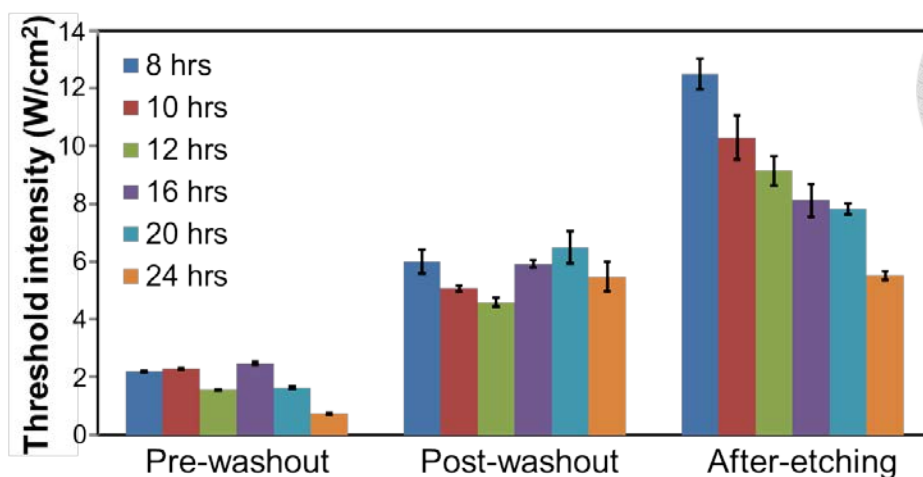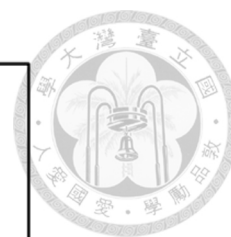
Fig. 3.10 Threshold laser intensities under the conditions of pre-washout, post-washout, and after-etching for various incubation times when NRI-AB is applied to the cell.
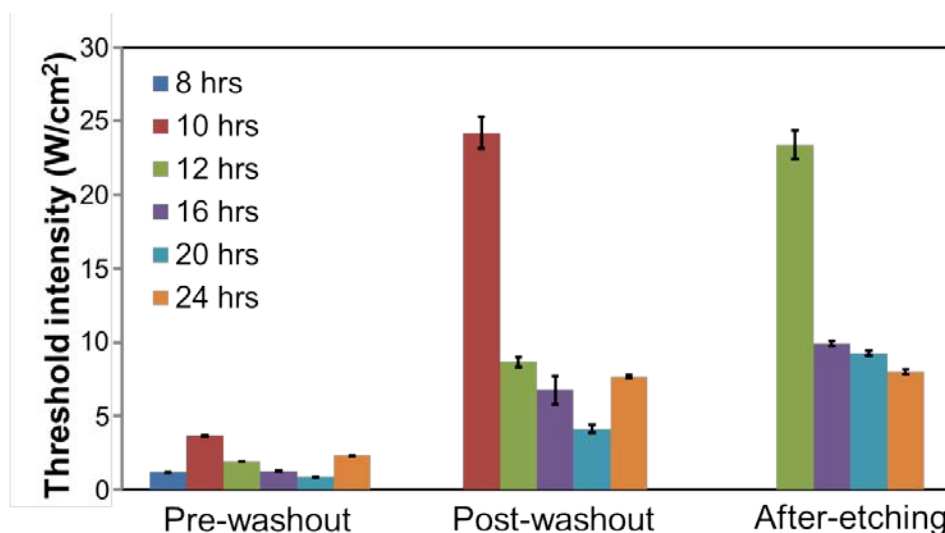

Fig. 3.11 Threshold laser intensities under the conditions of pre-washout, post-washout, and after-etching for various incubation times when NRI-control is applied to the cell.
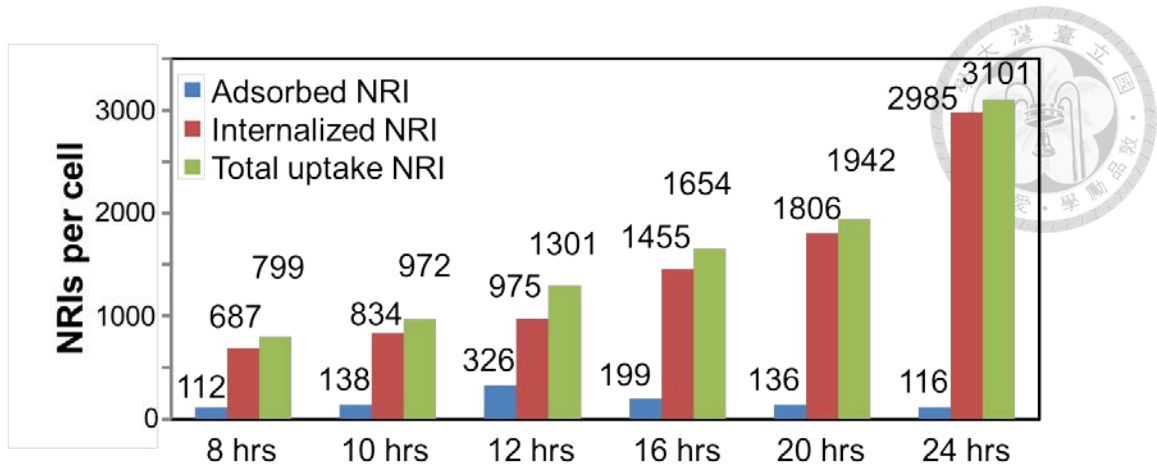
Fig. 3.12 Average NRI numbers per cell adsorbed and internalized, and their summation (total uptake NRI) with different incubation times when NRI-AB is used for cell inactivation experiment.
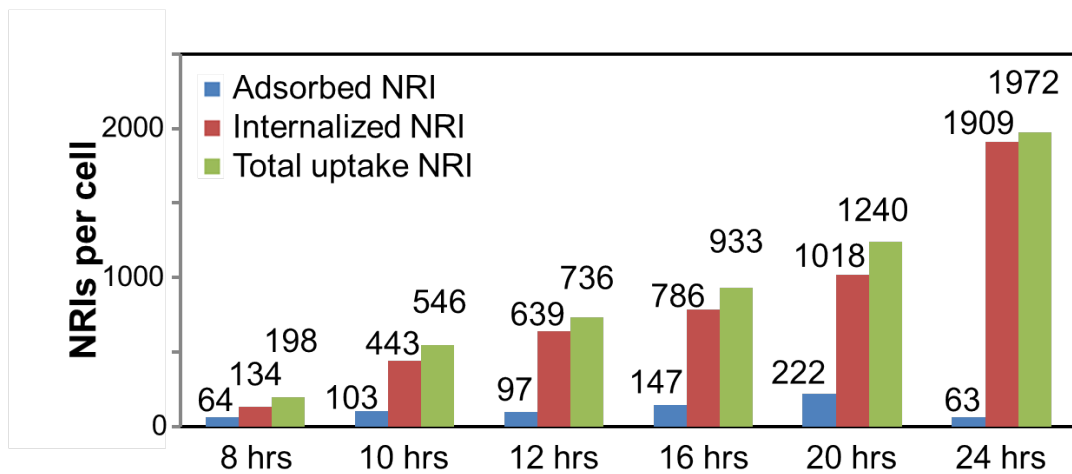

Fig. 3.13 Average NRI numbers per cell adsorbed and internalized, and their summation (total uptake NRI) with different incubation times when NRI-control is used for cell inactivation experiment.
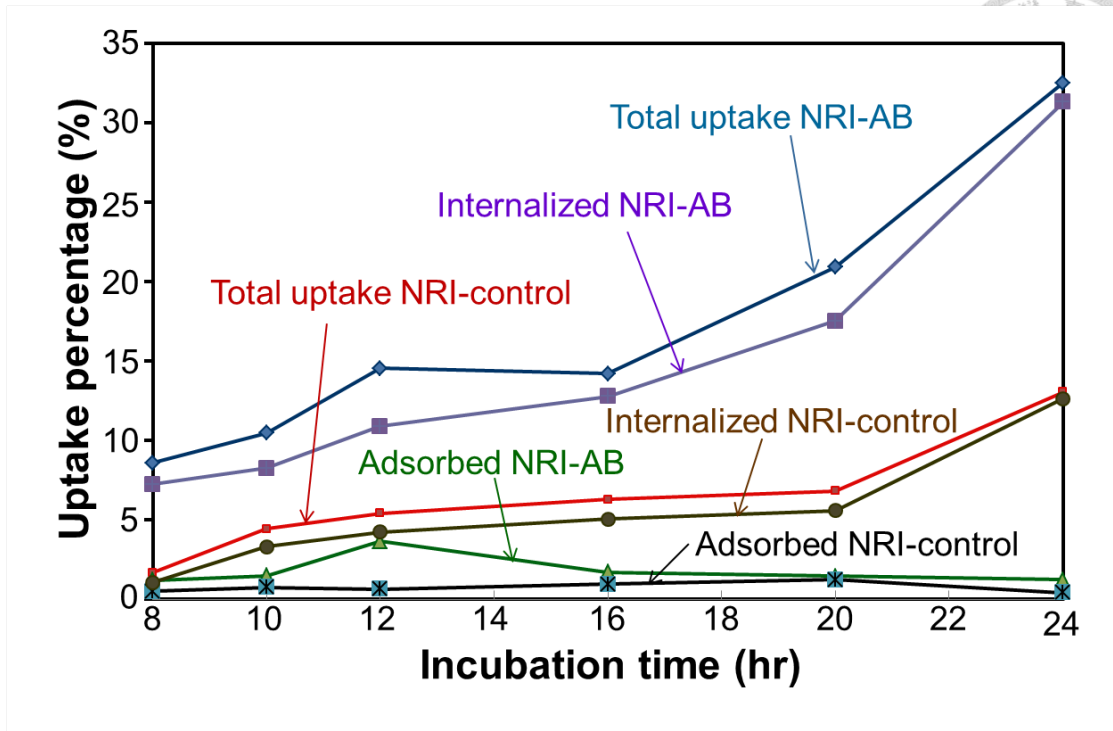
Fig. 3.14 Percentages of the adsorbed, internalized, and total uptake NRIs (the summation of the adsorbed and internalized NRIs) out of the applied NRIs for both cases of NRI-AB and NRI-control.

Chapter 4

Conclusions

In summary, we have applied Au NRIs, which have the LSP resonance wavelength around 1058 nm, either with linked antibody (NRI-AB) or without antibody (NRI-control), to SAS oral cancer cell for cell inactivation through the LSP-induced photothermal effect when it was illuminated by a laser of 1065 nm in wavelength. Various incubation times after the application of Au NRIs to the SAS cancer cell were considered for observing the variations of cell uptake of Au NRI and hence the threshold laser intensity for cancer cell inactivation. In each case of incubation time, the cell was washed for evaluating the Au NRI number per cell adsorbed and internalized by the cells. Also, the Au NRIs adsorbed (remaining on cell membrane) were etching with KI/I_2 to evaluate the Au NRI number per cell internalized by the cells. The threshold laser intensities before washout, after washout, and after KI/I_2 etching were calibrated from the circular area sizes of inactivated cells around the illuminated laser spot center under the illuminations of various laser power levels. The adsorbed and internalized Au NRIs per cell were obtained from ICP-MS measurements of the flushed solution in the KI/I_2 etching process and the remaining cells, respectively. By using Au NRIs

with antibody, it was found that the internalized Au NRI number per cell increased with incubation time. However, the adsorbed Au NRI number per cell reached a maximum at 12 hrs in incubation time. The cell uptake behaviors of Au NRIs without antibody were similar to those with antibody. Nevertheless, the NRI numbers per cell were significantly smaller. Meanwhile, the incubation time for the maximum adsorbed NRI number per cell was delayed to 20 hrs. By comparing the variation of threshold laser intensity for cell inactivation, it was found that the adsorbed NRIs could cause more effective cancer cell inactivation, when compared with the internalized NRIs. The minimum threshold laser intensities after washout in either case with or without antibody were observed before KI/I_2 etching under the aforementioned incubation time conditions of maximum adsorbed NRI number per cell.
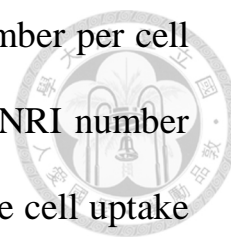
References

[1] K. L. Kelly et al., *J. Phys. Chem. B* **107**, 668 (2003).

[2] C. F. Bohren and D. R. Huffman, " Absorption and Scattering of Light by Small Particles", *John Wiley & Sons, Inc., New York, NY, 1st edition* (1983).

[3] M. C. Daniel and D. *Astruc, Chem. Rev.* **104**, 293 (2004).

[4] M. Eghtedari, A. V. Liopo, J. A. Copland, A. A. Oraevsky and M. Motamedi, *Nano Lett.* **9**, 287 (2009).

[5] W. I. Choi, J. Y. Kim, C. Kang, C. C. Byeon, Y. H. Kim, and G. Tae, *ACS Nano* **5**, 1995 (2011).

[6] G. von Maltzahn, J. H. Park, A. Agrawal, N. K. Bandaru, S. K. Das, M. J. Sailor, and S. N. Bhatia, *Cancer Res.* **69**, 3892 (2009).

[7] A. M. Gobin, J. J. Moon, and J. L. West, *Internal. J. Nanomed.* **3**, 351 (2008).

[8] A. M. Gobin, M. H. Lee, N. J. Halas, W. D. James, R. A. Drezek, and J. L. West, *Nano Lett.* **7**, 1929 (2007).

[9] L. B. Carpin, L. R. Bickford, G.Agollah, T. K. Yu, R. Schiff, Y. Li, and R. A. Drezek, *Breast Cancer Res. Treat.* **125**, 27 (2011).

[10] A. M. Schwartzberg, T. Y. Olson, C. E. Talley, and J. Z. Zhang, *J. Phys. Chem. B* **110**, 19935 (2006).

[11] J. Z. Zhang, *J. Phys. Chem. Lett.* **1**, 686 (2010).

[12] J. Chen, D. Wang, J. Xi, L. Au, A. Siekkinen, A. Warsen, Z. Y. Li, H. Zhang, Y. Xia, and X. Li, *Nano Lett.* **7**, 1318 (2007).

[13] J. Chen, F. Saeki, B. J. Wiley, H. Cang, M. J. Cobb, Z. Y. Li, L. Au, H. Zhang, M. B. Kimmey, X. Li, and Y. Xia, *Nano Lett.* **5**, 473 (2005).

[14] J. Chen, C. Glaus, R. Laforest, Q. Zhang, M. Yang, M. Gidding, M. J. Welch, and Y. Xia, *Small* **6**, 811 (2010).

[15] M. E. Brezinski, G. J. Tearney, B. E. Bouma, J. A. Izatt, M. R. Hee, E. A. Swanson, J. F. Southern, and J. G. Fujimoto, *Circulation* **93**, 1206 (1996).

[16] J. Turkevitch, P. C. Stevenson and J. Hillier, *Discuss. Faraday Soc.* **11**, 55 (1951).

[17] G. Schmid, R. Pfeil, R. Boese, F. Bandermann, S. Meyer, G. H. M. Calis and J. W. A. van der Velden, *Chem. Ber.* **114**, 3634 (1981).

[18] M. Brust, M. Walker, D. Bethell, D. J. Schiffrin and R. Whyman, *J. Chem. Soc., Chem. Commun.* **801** (1994).

[20] M. J. Hostetler, J. E. Wingate, C. J. Zhong, J. E. Harris, R. W. Vachet, M. R. Clark, J. D. Londono, S. J. Green, J. J. Stokes, G. D. Wignall, G. L. Glish, M. D. Porter, N. D. Evans and R. W. Murray, *Langmuir* **14**, 17 (1998).

[21] N. R. Jana, L. Gearheart and C. J. Murphy, *Chem. Mater.* **13**, 2313 (2001).

[22] S. Link, M. A. El-Sayed *J. Phys. Chem. B* **103,** 4212 (1999).

[23] U. Kreibig and M. Vollmer, *Optical Properties of Metal Clusters* Springer, Berlin (1995).

[24] R. Gans, *Ann. Phys.* **37**, 881 (1912).

[25] F. Kim, J. H. Song and P. D. Yang, *J. Am. Chem. Soc.* **124**, 14316 (2002).

[26] C. R. Martin, *Chem. Mater.* **8**, 1739 (1996).

[27] S. S. Chang, C. W. Shih, C. D. Chen, W. C. Lai and C. R. C. Wang, *Langmuir* **15**, 701 (1999).

[28] C. J. Murphy, T. K. Sau, A. M. Gole, C. J. Orendorff, J. X. Gao, L. F. Gou, S. E. Hunyadi and T. Li, *J. Phys. Chem. B* **109**, 13857 (2005).

[29] B. Nikoobakht, M. A. El-Sayed *Chem. Mater.* **15,** 1957 (2003).

[30] J. Aizpurua, P. Hanarp, D. S. Sutherland, M. Ka¨ll, G. W. Bryant, and F. J. Garcı´a de Abajo, *Phys. Rev. Lett.* **90**, 057401 (2003).

[31] F. Hao, E. M. Larsson, T. A. Ali, D. S. Sutherland and P. Nordlander, *Chem. Phys. Lett.* **458,** 262 (2008).

[32] E. M. Larsson, J. Alegret, M. K¨all and D. S. Sutherland, *Nano Lett.* **7**, 1256 (2007).

[33] H. Y. Tseng, C. K. Lee, S. Y. Wu, T. T. Chi, K. M. Yang, J. Y. Wang, Y. W. Kiang, C. C. Yang, M. T. Tsai, Y. C. Wu, H. Y. E. Chou, and C. P. Chiang, *Nanotechnology* **21**, 295102 (2010).

[34] C. K. Lee, H. Y. Tseng, C. Y. Lee, S. Y. Wu, T. T. Chi, K. M. Yang, H. Y. E. Chou, M. T. Tsai, J. Y. Wang, Y. W. Kiang, C. P. Chiang, and C.

C. Yang, *Biomed. Opt. Express* **1**, 1060-1074 (2010).

[35] H. Y. Tseng, W. F. Chen, Y. W. Kiang, and C. C. Yang, *Nanotechnology* **24**, 065102 (2013).

[36] S. Y. Wu, W. M. Chang, H. Y. Tseng, C. K. Lee, T. T. Chi, J. Y. Wang, Y. W. Kiang, and C. C. Yang, *Plasmonics* **6**, 547 (2011).

[37] H. G. Liu, Chang-Wei Wang, Jia-Pei Wua, Yong-Ill Leeb, Jingcheng Hao. *Colloids and Surfaces A: Physicochem. Eng. Aspects* **312,** 203 (2008).

[38] Y. Hu et al. *Proc. of SPIE* Vol. **8595,** 85950B-1-7 (2013).

[39] S. J. Tzlil, M. Deserno; W. M. Gelbart, J. Phys. Chem. B **106**, 5543 (2002).

[40] G. Bao; X. R. Bao *Proc. Natl. Acad. Sci. U.S.A.* 9997 (2005).

[41] B. D. Chithrani and W. C. W. Chan. *Nano Letter* **6**, 1542 (2007).

[42] X. Huang and M. A. El-Sayed, *J. Adv. Res.* **1**, 13 (2010).

[43] X. Huang, I. H. El-Sayed, W. Qianand, and M. A. El-Sayed, *J. Am. Chem. Soc.* **128**, 2115 (2006).

[44] S. Lal, S. E. Clareand, and N. J. Halas, *Acc. Chem. Res.* **41**, 1842 (2008).

[45] S. Jelveh and D. B. Chithrani, *Cancers* **3**, 1081 (2011).

[46] E. S. Day, J. G. Morton, and J. L. West, *J. Biomech. Eng.* **131**, 074001 (2009).

[47] X. Huang, P. K. Jain, I. H. El-Sayed, and M. A. El-Sayed, *Photochem Photobiol.* **82**, 412 (2006).

[48] B. Jang, J. Y. Park, C. H. Tung, I. H. Kim, and Y. Choi, *ACS Nano* **5**, 1086 (2011).

[49] R. J. Bernardi, A. R. Lowery, P. A. Thompson, S. M. Blaney, and J. L. West, *J. Neurooncol.* **86**, 165 (2008).

[50] R. Chen, X. Zheng, H. Qian, X. Wang, J. Wang, and X. Jiang, *Biomater. Sci.* DOI: 10.1039/C2BM00138A (2013).

[51] H. Liu, D. Chen, L. Li, T. Liu, L. Tan, X. Wu, and F. Tang, *Angew Chem Int Ed Engl.* **50**, 891 (2011).

[52] S. Link and M. A. El-Sayed, *J. Phys. Chem. B* **103**, 42127 (1999).

[53] M. E. Brezinski, G. J. Tearney, B. E. Bouma, J. A. Izatt, M. R. Hee, E. A. Swanson, J. F. Southern, and J. G. Fujimoto, *Circulation* **93**, 1206 (1996).

[54] L. R. Hirsch, R. J. Stafford, J. A. Bankson, S. R. Sershen, B. Rivera, R. E. Price, J. D. Hazle, N. J. Halas, and J. L. West, *PNAS* **100**, 13549 (2003).

[55] B. Jang, J. Y. Park, C. H. Tung, I. H. Kim, and Y. Choi, *ACS Nano* **5**, 1086-1094 (2011).

[56] J. M. Tucker-Schwartz, T. A. Meyer, C. A. Patil, C. L. Duvall, and M. C. Skala, *Biomed. Opt. Express* **3**, 2881 (2012).

[57] K. Sokolov, M. Follen, J. Aaron, I. Pavlova, A. Malpica, R. Lotan,

and R. Richards-Kortum, *Cancer Research* **63,** 1999 (2003).

[58] H. Muamatsu, K. Kogawa, T. Kuga, and Y. Niitsu, *Cancer Res.***55**, 6210 (1995).

[59] S. Shinriki, H. Jono, K. Ota, *Clinical Cancer Res.***15**, 5426 (2009).

[60] Shih-Hwa Chiou, Cheng-Chia Yu, Chi-Yang Huang, *Clinical Cancer Res.***14**, 4085 (2008).